

EXPERIMENTAL CHARACTERIZATION AND NUMERICAL MODELING OF
ADDITIVE-MANUFACTURED COMPOSITE SOLID ROCKET
PROPELLANT WITH ANISOTROPIC DENSITY

by
Cameron Brown

© Copyright by Cameron Brown, 2019

All Rights Reserved

A thesis submitted to the Faculty and the Board of Trustees of the Colorado School of Mines in partial fulfillment of the requirements for the degree of Master of Science (Materials Science).

Golden, Colorado

Date _____

Signed: _____
Cameron Brown

Signed: _____
Dr. Sridhar Seetharaman
Thesis Advisor

Signed: _____
Tim Bulk
Thesis Advisor

Golden, Colorado

Date _____

Signed: _____
Dr. Ryan O'Hayre
Professor and Program Director,
Department of Metallurgical and Materials Engineering

ABSTRACT

Additive manufacturing (AM) allows for fabrication of functionally-graded energetic materials such as solid rocket propellant. Significant improvements in grain geometry control and burn rate manipulation may be realizable, but new defects unique to AM processes must be characterized to understand their influence on material performance.

The objective of this thesis research is to characterize defects in 3D-printed ammonium perchlorate composite propellant (APCP) related to processing conditions and model their effect on deflagration. X-ray photoelectron spectroscopy (XPS) and x-ray computed tomography (XCT) analysis methods are used to quantify binder photopolymerization and porosity in the build direction, respectively. A model is developed to predict degree of polymerization as a function of depth and experimental data are fit. XCT imaging results indicate that porosity in 3D-printed APCP is attributed to poor inter-layer adhesion and binder phase separation. The slow powder burn equation of state available in ANSYS Autodyn hydrocode software is used to model APCP deflagration as a function of the experimental porosity data, but model results were not compared to experimental closed-bomb data in this research. Results repeatability would be improved in future embodiments of this research that analyze higher-quality 3D-printed APCP samples.

TABLE OF CONTENTS

ABSTRACT	iii
LIST OF FIGURES	vi
LIST OF TABLES	viii
LIST OF SYMBOLS	ix
LIST OF ABBREVIATIONS	x
ACKNOWLEDGMENTS	xii
CHAPTER 1 INTRODUCTION	1
1.1 Rocket Propellant Overview	1
1.2 Additive Manufacturing Application to SRMs	4
1.3 Thesis Objectives	6
CHAPTER 2 XPS ANALYSIS OF BINDER PHOTOPOLYMERIZATION IN ADDITIVE-MANUFACTURED SRMS	9
2.1 Energetics AM Processes	9
2.2 XPS Overview	13
2.3 Sample Preparation	14
2.4 Experimental Procedure	17
2.5 Results	18
2.6 Discussion	20
2.7 XPS Conclusions	26
CHAPTER 3 X-RAY COMPUTED TOMOGRAPHY ANALYSIS OF 3D-PRINTED SRM SAMPLES	27

3.1	XCT Overview	27
3.2	Sample Preparation and Experimental Procedure	28
3.3	Results	30
3.4	Discussion	33
3.5	XCT Conclusions	35
CHAPTER 4 NUMERICAL MODELING OF POROSITY-GRADED 3D-PRINTED SRMS		37
4.1	Propellant Deflagration Modeling in ANSYS Autodyn	37
4.2	Modeling homogeneous APCP propellant with variable burn rate	41
4.3	Propellant modeling limitations in Autodyn	44
4.4	Modeling porosity-graded propellant	47
4.5	Summary of Modeling Assumptions	53
4.6	Numerical Modeling Conclusions	55
CHAPTER 5 CONCLUSIONS		57
REFERENCES CITED		61

LIST OF FIGURES

Figure 1.1	Basic diagram of a SRM showing the propellant, insulation and casing, igniter, and nozzle.	1
Figure 1.2	Example SRM grain geometries and corresponding thrust profiles.	2
Figure 1.3	Cross-section of cast HTPB-based solid propellant.	3
Figure 1.4	Computer-aided design image renderings of 3D-printable SRM grain geometries and theorized resultant thrust profiles based on linear grain regression from grain center.	5
Figure 1.5	High-level overview of thesis research topics.	7
Figure 2.1	Photopolymerization gradients inherent in robocasting UV-cure AM	13
Figure 2.2	PEGDA oligomers used as the binder in printed APCP motors	14
Figure 2.3	3D-printed APCP SRM sample preparation for XPS analysis	16
Figure 2.4	Experimental XPS results of C 1s spectra concentrations	19
Figure 2.5	Highlighted C=C bond area in curve-fit data for C 1s spectra	20
Figure 2.6	Normalized experimental DOP values calculated by equation 2.1	24
Figure 3.1	Hypothesized sequential porosity defects in 3D-printed APCP SRMs attributed to inter-layer delamination.	28
Figure 3.2	Printed APCP SRM sample preparation for XCT analysis.	29
Figure 3.3	XCT image of 3D-printed APCP SRM sample and cross-sectional plane. . .	31
Figure 3.4	Plane alignment procedure for histographic segmentation of samples. . . .	32
Figure 3.5	Porosity data for 3D-printed APCP SRM scans 021419 and 031219.	32
Figure 3.6	Highlighted PEGDA binder in a cross-sectional plane parallel to the build direction in sample 031219.	33

Figure 3.7	Porosity and binder concentration data from XCT scan 031219.	35
Figure 4.1	Visual representation of unit cell volume composed of solid and gaseous propellant.	38
Figure 4.2	Analytical calculation by Atwood displaying density changes of phases during combustion.	40
Figure 4.3	Least-squares fit of Vieille’s law constants for experimental APCP closed-bomb burning test data.	43
Figure 4.4	Comparison of convective and conductive burning mechanisms on gas pressure and reaction rate in APCP.	46
Figure 4.5	Single layer segment of 031219 XCT porosity data used for Autodyn mesh generation.	48
Figure 4.6	Flame front propagation over porous and solid infill APCP.	50
Figure 4.7	Gas pressure, burn rate, and flame front acceleration comparison plots for porous and solid infill APCP.	52

LIST OF TABLES

Table 2.1	Formulation of the APCP motor printed by SAS and used for XPS analysis.	15
Table 2.2	CASA XPS data fit parameters for C 1s spectra components.	18
Table 3.1	XCT analysis settings	30
Table 4.1	Experimental APCP burn rate and pressure data	41
Table 4.2	Least-squares fit APCP burn rate and pressure data input to Autodyn slow powder burn EOS	44
Table 4.3	APCP material data for input to Autodyn	49
Table 4.4	Autodyn simulation setup parameters	49

LIST OF SYMBOLS

XPS Nomenclature

Carbon 1s Orbital Electron Shell	$C1s$
Free Radical Concentration	$[M^*]$
Monomer Concentration at Depth l	$[M]$
Steady-State Monomer Concentration at Surface	$[M_s]$

Numerical Modeling Nomenclature

Average Density of Gaseous Phase in Total Cell Volume	$\bar{\rho}_g(t)$
Average Density of Solid Phase in the Total Cell Volume	$\bar{\rho}_s(t)$
Combined Density of Solid and Gaseous Phases in Cell	$\rho(t)$
Conductive Burning Rate	\dot{b}
Convective Burn Front Velocity	v
Density Scaling Constant	C_2
Extended Vielle's Law Constant	c
Gas Pressure	P_g
Mass of Gaseous Phase in Cell	$M_g(t)$
Propellant Gaseous Phase Density	$\rho_g(t)$
Propellant Solid Phase Density	$\rho_s(t)$
Reaction Ratio	F
Vielle's Law Pressure Exponent	n

LIST OF ABBREVIATIONS

Activation Energy	<i>E_a</i>
Additive Manufacturing	AM
Ammonium Perchlorate Composite Propellant	APCP
Bis Acyl Phosphine	BAPO
Computational Fluid Dynamics	CFD
Courant-Friedrichs-Lewy	CFL
Degree of Polymerization	DOP
Equation of State	EOS
Full Width at Half Max	FWHM
Fused Deposition Modeling	FDM
High Explosive	HE
Hydroxyl-Terminated Polybutadiene	HTPB
Liquid Rocket Engine	LRE
Poly(Ethylene Glycol) Diacrylate	PEGDA
Selective Laser Sintering	SLS
Solid Rocket Motor	SRM
Stereolithography	SLA
Theoretical Maximum Density	TMD
Ultraviolet	UV
X-ray Computed Tomography	XCT

X-ray Photoelectron Spectroscopy XPS

ACKNOWLEDGMENTS

I would like to acknowledge Special Aerospace Services for funding my energetics additive manufacturing research the past few years and now for funding this thesis research. This research would not have been possible without the support of my advisor, Dr. Sridhar Seetharaman (professor, CSM), and without the technical support of Dr. Kenneth Steirer (research assistant professor, CSM) during the materials characterization testing. I am thankful for the propellant modeling guidance given by Paul Braithwaite (senior staff scientist, Northrop Grumman Corporation), research input by Dr. Geoff Brennecka (assistant professor, CSM) and the Autodyn modeling help given by Eduardo Lozano (PhD candidate, CSM).

CHAPTER 1

INTRODUCTION

1.1 Rocket Propellant Overview

Solid rocket propellant is a composite energetic material commonly used in aerospace or military applications where thrust is required to propel a payload. When utilized as a propulsive device on a vehicle the propellant is often referred to as a Solid Rocket Motor (SRM). In contrast to Liquid Rocket Engines (LREs), SRMs are regarded as one of the most reliable aerospace propulsion systems because of their simplicity and lack of moving components. However, SRMs are not throttleable like LREs and the geometry of the cast solid propellant has a large impact on motor performance. During combustion, solid propellant burns radially outward from any surface in contact with the flame zone. The hot gaseous combustion products increase the chamber pressure and are expelled out of the SRM via the nozzle. The conversion from potential energy to thermal energy to kinetic energy in the SRM creates thrust which can be used to propel a payload. Figure 1.1 [1] below shows a basic schematic of SRM components. Note that composite materials are often used in place of metal casing for weight savings.

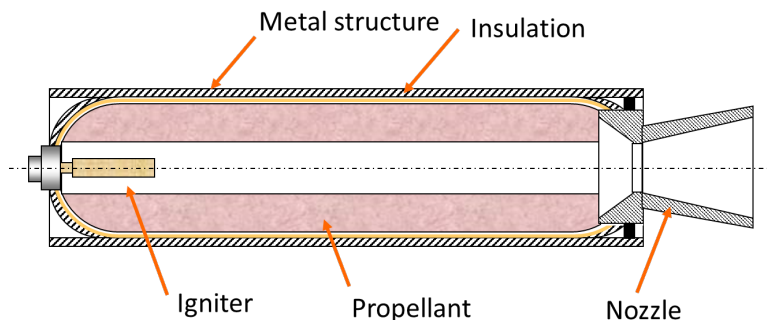


Figure 1.1: Basic diagram of a SRM showing the propellant, insulation and casing, igniter, and nozzle.

The surface area exposed to the flame zone at any point during combustion determines the thrust output of the motor. Altering the cross-sectional geometry of the motor changes the propellant surface area exposed to the flame zone throughout combustion and thus alters the thrust output of the SRM. Example geometries and corresponding thrust profiles associated with commonly cored-out of cast SRMs are shown below in Figure 1.2 [2].

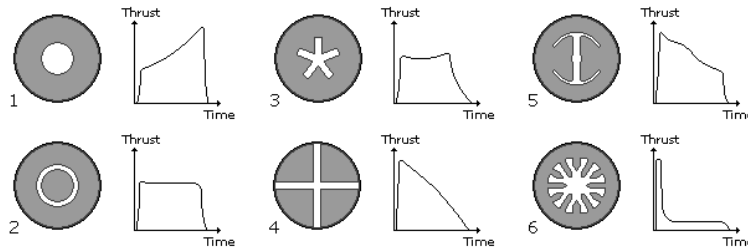


Figure 1.14

Figure 1.2: Example SRM grain geometries and corresponding thrust profiles. The cross-sectional grain geometry of SRMs changes the thrust profile of the motor as the propellant regresses normal to the burning surface during deflagration.

In this document "grain" is synonymous with solid propellant. Grain geometry design is especially important in space launch vehicle SRMs where ambient pressure and launch vehicle mass change considerably during flight. At high altitudes SRM nozzles become under expanded due to low ambient pressure and SRM efficiency plummets. Additionally, the maximum dynamic pressure that a vehicle sustains can be altered by changing the SRM booster grain geometry; high accelerations caused by large booster thrust output cause higher maximum dynamic pressures that can have a damaging impact on the launch vehicle and/or payload.

Solid rocket propellant is composed of oxidizer and fuel constituents that when mixed together enable sustained combustion. Together, the fuel and oxidizer facilitate a redox reaction. Upon combustion the oxidizer is reduced (it gains electrons) and the fuel is oxidized (it loses electrons). This redox reaction is the basis of propellant deflagration. However, since the oxidizer and fuel are mixed together during manufacturing, a SRM cannot be extinguished after ignition. This lack of motor throttle control often means that SRM ignition

is among one of the last steps in a vehicle launch sequence. When used as boosters on the space shuttle, SRMs were only ignited after ignition of the LREs was verified [3]; the shuttle launch could be aborted after LRE ignition but not after SRM ignition.

Traditionally, SRMs are manufactured via a casting process where propellant is pre-mixed and poured under vacuum into a mold where it cures. Grain geometry is selected and prepared by boring out through the curing propellant or using removable cores based on thrust requirements of the motor. Although casting is the industry standard, it is rudimentary as it leaves little design flexibility because SRM performance is constrained to simple castable grain patterns and as a result, the material performance is severely limited. Manufacturing defects, polymer binder cure kinetics, and curing agent gas evolution also occur during casting which lead to unpredictable motor performance and potentially hazardous situations for personnel. These imperfections are a result of lack of control of the structure on and below the mesoscale (100 - 5,000 μm) region [4] during manufacturing. Voids are often unintentionally introduced to the grain during manufacturing which result in reduced fractions of Theoretical Maximum Density (TMD) [2]. Figure 1.3 below shows a cross section of cast Hydroxyl-Terminated Polybutadiene (HTPB) solid propellant [5].

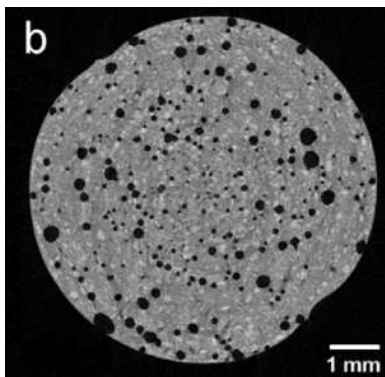


Figure 1.3: Cross-section of cast HTPB-based solid propellant. Random porosity in the cast propellant is detrimental to performance and causes perturbations in burn rate.

The random porosity of the material incurred through manufacturing processes is especially relevant to high explosives (HEs); voids in the material form “hot spots” during

detonation and cause localized detonation energy increases that are unpredictable [6].

1.2 Additive Manufacturing Application to SRMs

Recent research started to investigate Additive Manufacturing (AM) as an alternative process for fabricating energetic materials. In contrast to subtractive machining processes such as lathing and milling, AM adds sequential layers of materials until a component is fabricated rather than removing material to form a component. Liquid rocket engine injectors and combustion chambers have been additive-manufactured, or “printed,” and successfully implemented in propulsion systems where conventional manufacturing cannot be used because of the design complexity and/or high manufacturing costs.

AM processes were reportedly initially used to produce energetic materials as early as 2000 [7]. Initial energetic materials AM efforts focused on developing printable “inks” for use with robocasting systems [8]. Commonly used printable inks are a solution of nanoenergetics (such as thermite powders) dispersed in a solvent. This initial research was largely motivated by Department of Defense (DoD) interest in developing “functionally-graded” energetic materials [9]. A functionally-graded material is heterogeneous in composition and structure, and designed for a specific application. Developing functionally-graded energetic materials using traditional casting techniques is impractical because the manufacturer must be able to control the material structure and composition at or below the mesoscale range. Similar to solid rocket propellant, pyrotechnics and gun propellants are energetic materials with burn rates that are dependent on grain geometry; control of the meso/microstructure of these materials and the ability to design tailored energetic materials is becoming increasingly important in DoD Research and Design programs. The development of 3D-printed gun propellants is motivated by the need for high-performance propellants that deliver high projectile velocities while lowering muzzle wear by reducing peak pressure [10]. AM processes could be used to tailor the grain geometry of gun propellants such that the pressure profile inside a gun muzzle after ignition is stabilized, delivering higher energy on target while reducing muzzle wear.

Functionally, gun propellants and SRMs are very similar. In each, a flame front encounters the propellant grain, the grain regresses normal to the flame zone as combustion progresses, and the thermal energy produced during combustion is converted to kinetic energy to propel a payload. However, gun propellants typically include higher energy density constituents such as nitramines, nitrocellulose and nitroglycerin, pressures inside a gun breech is much higher than the pressure inside a SRM, and as a result gun propellant combustion occurs over several milliseconds while the projectile is still accelerating inside the gun muzzle, whereas SRMs typically burn for several seconds or even minutes. Despite these differences, SRMs are candidates for implementation of AM processes as well.

In contrast to cast SRMs which have a constant cross-sectional grain geometry along the length of the motor, a printed motor could have dynamic cross-sectional grain geometry along its length as shown below in Figure 1.4.

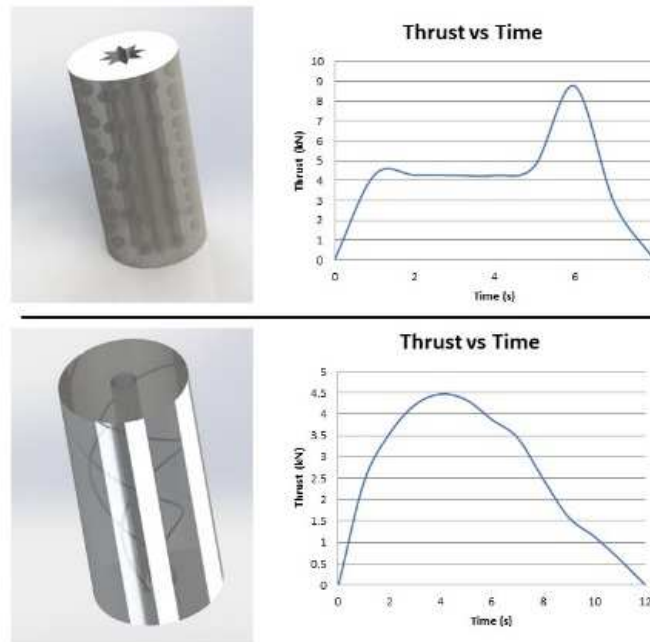


Figure 1.4: Computer-aided design image renderings of 3D-printable SRM grain geometries and theorized resultant thrust profiles based on linear grain regression from grain center. 3D printing allows for the design of complex geometries and tailored SRM thrust profiles.

AM also allows for the use of multiple materials during fabrication of a single component. Different energy density variant materials could be incorporated into a SRM for additional control and alteration of the motor's thrust. Safety concerns during SRM manufacturing are paramount and increase production costs. Facilities that are equipped to manufacture propellant and cast it must meet extensive and necessary safety precautions to ensure that propellant exposure and ignition risks are mitigated for personnel handling the propellant. In contrast, AM can be performed remotely so personnel are not at risk during the manufacturing process. The isolated and fully autonomous nature of additive manufacturing also means that manufacturing costs due to safety regulation compliance and labor costs are reduced.

Military interest also stems from the rapid "speed to fleet" potential of energetics AM and the ease of manufacturing for limited production run SRMs. Fully autonomous AM decreases production times of rocket motors because motor production can begin immediately following the engineering design phase. No mold is needed to produce a 3D-printed SRM, so no manufacturing costs associated with mold design or fixturing are incurred. Limited production run 3D-printed SRMs don't see high manufacturing costs due to non-recurring expenses such as mold design and setup, and new innovative energetic products can be rapidly produced and brought into service with significantly reduced lead times and costs.

1.3 Thesis Objectives

The objective of this thesis research is to characterize defects in 3D-printed Ammonium Perchlorate Composite Propellant (APCP) SRMs related to processing conditions and predict their effect on performance. Two forms of material characterization testing were performed on 3D-printed APCP samples, X-ray Photoelectron Spectroscopy (XPS) and X-ray Computed Tomography (XCT). XPS testing was performed to quantify the Degree of Polymerization (DOP) of the Ultraviolet (UV)-curable binder photopolymer constituent in the propellant formulation. XCT imaging was performed to quantify the porosity inherent in 3D-printed SRM samples as a result of manufacturing defects. The porosity results were

then considered in the numerical modeling of APCP deflagration. ANSYS Autodyn software was utilized to develop the explicit dynamics simulations that predicted the transient burn rate and pressure profiles of printable SRMs as a function of as-printed density and propellant formulation. A high-level depiction of material characterization research completed in this thesis is shown below in Figure 1.5.

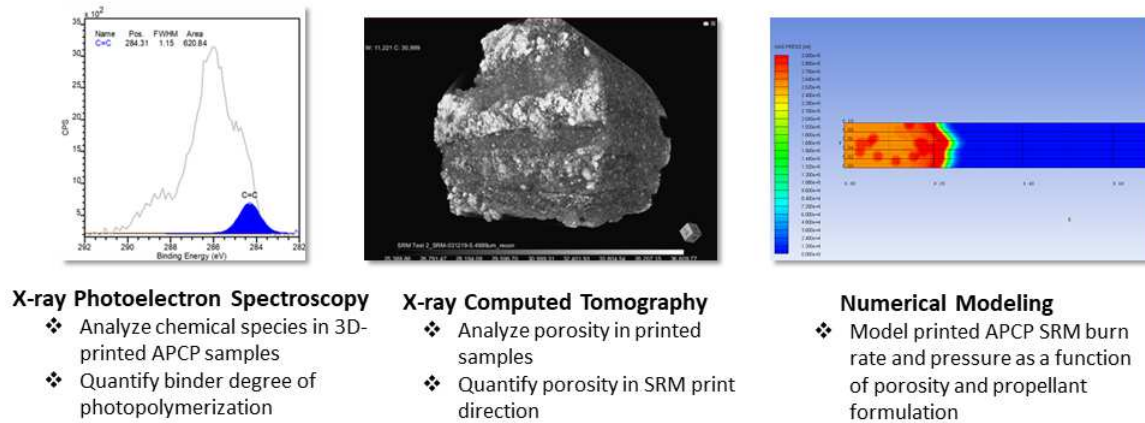


Figure 1.5: High-level overview of thesis research topics. XPS and XCT material characterization methods were utilized to quantify defects in 3D-printed APCP samples. Results from both testing methods were used to model APCP deflagration in ANSYS Autodyn software.

The motivations for each of the three material characterization subjects in this thesis are briefly described here. It was hypothesized that if insufficient UV power was transmitted to the APCP slurry during printing that a DOP gradient would exist in each deposited and cured layer of material and furthermore that a low DOP at the bottom of layers would cause inadequate inter-layer adhesion and delamination. Additionally it was hypothesized that layer delamination in samples was responsible for meso/microscale porosity defects measurable with XCT instrumentation.

Chapter 2 begins with a subsection on AM methods and challenges applicable to energetic materials. Subsequent sections in chapter 2 discuss XPS analysis of 3D-printed APCP samples. The results from the XPS testing are considered in the analysis of sample meso/microstructure in chapter 3. Porosity data gathered from XCT testing are then used to define the Eulerian mesh setup in a Autodyn simulation of flame front propagation through a 1

mm layer of APCP in chapter 4 subsection 4.4.

3D-printed APCP samples used for XPS and XCT testing were provided by Special Aerospace Services (SAS). Although an overview of energetics AM processes is given in subsection 2.1, complete details of the AM process used by SAS for sample printing are not provided. Any details included in this thesis regarding the propellant formulation and printing processes can be found in subsection 2.3. This research is intended primarily to be an exploratory effort to characterize anisotropic properties of 3D-printed energetic materials in the newly-emerging field of energetics AM.

CHAPTER 2
XPS ANALYSIS OF BINDER PHOTOPOLYMERIZATION IN
ADDITIVE-MANUFACTURED SRMS

The purpose of this chapter is to describe how XPS was used to quantify the DOP of SRMs printed via robocasting and UV-curing. Propellant grains with low DOP have insufficient structural integrity and are hypothesized to increase porosity between layers. The DOP is quantified in this chapter and the data are used as supporting evidence for porosity defect modes discussed in chapter 3. Before the XPS analysis is described, a brief overview of energetics AM processes and challenges is given.

2.1 Energetics AM Processes

Commonly used cast propellant formulations include Ammonium Perchlorate (AP) oxidizer as a solid phase, aluminum powder as a high-energy fuel solid phase, and HTPB binder as the thermoset curable liquid polymer phase. When solid and liquid constituents are combined in a stoichiometric 85:15 ratio by mass, a slurry is formed with viscosity up to 69 million cP [5]. AM of composite rocket propellants is notoriously difficult because stoichiometric propellant formulations have high loading ratios of solid to liquid constituents.

APCP AM is difficult with Fused Deposition Modeling (FDM) processes because the thermoplastic filament utilized in FDM printing cannot be loaded with 85% solid particulates and extruded successfully from the FDM printer. As the solids loading in the liquid phase increases, the viscosity of the composite mixture similarly increases. The high molecular weight of thermoplastic 3D printing filaments such as Poly(lactic) Acid (50 – 100 PaS) [11] relative to HTPB (5 PaS at 30°C)[12] prevent the thermoplastic filaments from being processable at low extrusion pressures common in FDM pressures if they are loaded with a high percentage of solid particulates. Incorporating polymodal particle distributions for solid constituents to increase the polydispersity index will reduce the viscosity of the mixture and enable higher

volumetric solids loading [13]. However, at higher solid loading ratios the viscosity of the thermoplastic filament and polymodal APCP solid constituents would increase to a point where the mixture would not be processable, and the viscosity would be similar to that of a solid material.

Thermoplastic filaments are heated above their glass transition temperature to lower their viscosity and enable extrusion from the 3D printer nozzle. If the filament is too viscous due to insufficient temperature or particulate clogging, the filament cannot be extruded from the printer nozzle. Thermoplastic filaments loaded with any quantity of APCP solid constituents would have a higher viscosity relatively to an un-loaded thermoplastic filament. This increase in viscosity necessitates higher extrusion pressure and temperature to force the composite material out of the printer nozzle. Similar to the viscosity-driven mixing limit described in the previous paragraph, an extrusion parameter limit exists for the FDM 3D printer utilized; the printer has a maximum extrusion pressure and temperature limited by its hardware. Mulage demonstrated successful processing of thermoplastic filament loaded with up to 90 wt.% APCP solid constituents, however binder solvation was required to load the thermoplastic to such high solids ratios, and a 60 T vertical press was required to extrude the propellant into the desired form [14]. The non-Newtonian shear-thinning properties of polymers help reduce the viscosity of the mixture during extrusion at higher pressures, but the viscosity reduction from shear-thinning and increased processing temperature is still above the practical limit for extrusion on Commercial-Off-The-Shelf (COTS) 3D printers at low solids loadings. In past research, the author found experimentally that PLA filaments could not be loaded with more than 30 wt.% AP particulates by heating the filament alone (no induced shear or processing solvents), and that filaments with more than 20 wt.% AP particulates could not be extruded using COTS thermoplastic 3D printers.

Also imperative in the design of an energetics AM system is the consideration of chemical degradation at higher processing temperatures. PLA filament is commonly heated to around $185^{\circ}C - 205^{\circ}C$ [15] in the printer nozzle to reduce the viscosity of the filament such that it

can be extruded. However, thermal degradation of PLA begins around 200°C , depending on polymer molecular weight, oxidative effects, and other factors [12]. Therefore, the workable design space for thermoplastic filaments loaded with solid particulates is exceedingly small; only a small addition of solid particulates to the filament is possible such that the increase in processing temperature to lower the viscosity is minimal, and thermal degradation of the polymer is mitigated. The elevated temperatures and extrusion pressures in FDM may also be a safety concern; autoignition temperatures at higher pressures need to be well understood so that the material does not ignite while printing.

Stereolithography (SLA) printing could be considered for SRM manufacturing, but SLA requires that the photopolymer resin used must have a low viscosity. The resin is UV-curable, meaning layers of the resin are cured into a solidified form within seconds of exposure to UV light. After each layer is printed, the part build platform is raised or lowered slightly in the vat of resin. If the resin is too viscous, air pockets are formed during the build platform adjustment step, and subsequent layers are printed with defects or fail altogether. The viscous paste consistency of pre-cured composite propellants cannot practically be utilized in SLA resin printers without the addition of significant quantities of solvents to reduce the viscosity. However, a large addition of organic solvents to the propellant mixture would greatly increase safety hazards, and create processing problems due to insufficient photopolymer curing and increased porosity in printed SRMs after solvent evaporation.

Selective Laser Sintering (SLS) printing has been demonstrated for AM of SRMs with sucrose/potassium nitrate formulations [16]. However, processing difficulties for SLS of APCP SRMs would be similar to those inherent in APCP FDM printing. If a thermoplastic binder were used for SLS printing, sintering the solid powder mixture of fuel and oxidizer constituents in an attempt to melt the thermoplastic binder to the metal powder and AP particles would be unsuccessful. Just as in FDM processes, a higher solids loading necessitates higher processing temperatures to reduce the viscosity of the mixture below a workable limit. Sintering a thermoplastic binder surrounded by a high content of solid metal powder and

oxidizer particles would cause thermal degradation of the thermoplastic binder before the binder's viscosity is reduced such that it disperses to bind surrounding solid particles into a composite matrix. Perhaps the most obvious challenge in utilizing SLS processes for AM of SRMs is safety; concentrating an energy source at a spot on a bed of energetic material introduces safety hazards that make SLS an impractical method of energetics AM if they are not mitigated.

The final SRM AM technical challenge discussed in this research is the importance of binder compatibility with other solid particulates and phase separation. During processing, the binder used must adhere sufficiently to the surrounding solid phase particulates. If a large enough difference in surface energy exists between the binder and surrounding particulates, phase separation may occur. In casting processes where HTPB curing occurs over several days, the primary mechanism for phase separation is diffusion; chemical potential gradients between the binder and surrounding phases drive the binder out of solution. Phase separation results in porosity in the SRM and reduced structural integrity of the grain due to increased heterogeneity. In energetics AM processes such as robocasting, a composite slurry of solid particulates and liquid phase binder is pressurized and extruded from a printer nozzle. Phase separation during robocasting is primarily due to advective transport and occurs orders of magnitude quicker than diffusion-driven phase separation.

Special consideration must be given to binder wettability when extrusion-based energetics AM processes are used; binder phase separation can occur rapidly, and the region from which the binder leaves increases in viscosity because less liquid phase is present. A localized increase in viscosity results in increased backpressure, which subsequently increases pressure in the surrounding regions, and increases phase separation. Incompatible binder selection can result in phase separation, nozzle clogging, and part failure. Surfactants (wetting agents) can be added to the formulation to reduce the surface tension between the liquid and solid interface and reduce the likelihood of phase separation during processing. Additionally, a larger polymer matrix entangled with many solid particulates is more likely to stay in

pressurized solutions than smaller molecular weight polymers.

For further information regarding propellant rheology, propellant processing fluid dynamics, and energetic materials AM challenges the author recommends “Energetic Materials: Advanced Processing Technologies for Next-Generation Materials” [7].

2.2 XPS Overview

Similar to robocasting, the AM system used in this research extrudes a composite slurry material from a nozzle in an additive, layer-by-layer process. As each layer is deposited, an ultraviolet LED array projected on the material initiates polymerization of the photopolymer binder in the slurry. This slurry deposition and UV-curing process is repeated until the entire energetic material sample is “printed”. A high-level overview of the energetic material AM process utilized in this research is shown below in Figure 2.1. When subjecting a layer to UV radiation for a certain time, the DOP depends on the kinetics of polymerization and the UV intensity. Since the intensity of the UV radiation decays with depth through a material, the DOP consequently varies.

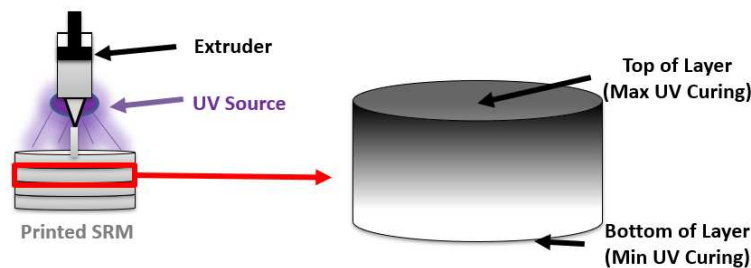


Figure 2.1: Photopolymerization gradients inherent in robocasting UV-cure AM. A High-level overview of energetic material additive manufacturing process is shown. The cylindrical APCP SRM printed for this research had layers 1 mm thick, and an outer diameter of 30 mm . Typical layer heights for energetic materials robocasting processes may range from $.1\text{ mm}$ to 1 mm , depending on printer dimensional accuracy limitations and allowable dimensional accuracy limitations for the printed SRM.

In order to manufacture energetic samples with consistent inter-layer polymerization and reasonable isotropy, binder polymerization must be characterized in terms of UV penetration depth and cure time. Polymerization gradients in printed layers lead to structural instability,

and anisotropic burning. Additionally, small-scale burn tests of printed samples indicate that the flame zone propagates faster at lower binder polymerization areas of the material than higher binder polymerization areas.

When a photosensitive molecule absorbs UV-wavelength photons a free radical molecule species is formed. The free radical then binds itself to an acrylate end chain and cleaves the C=C double bonds [17]. Below, Figure 2.2 shows the bond line structure for poly(ethylene glycol) diacrylate (PEGDA) photopolymer used in this research. The majority of the C-C and C-O-C bonds present in samples will reside in the polyethylene glycol backbone; C=O, O-C=O, and C=C bonds reside in the acrylate end groups.

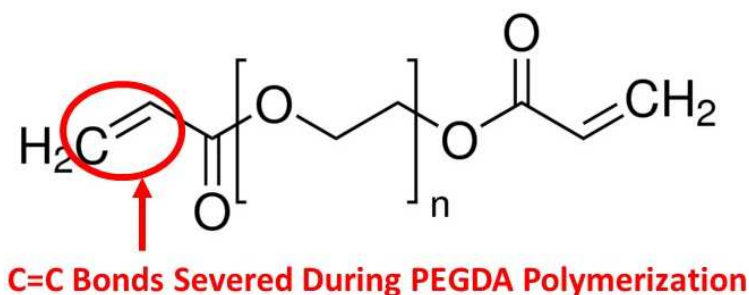


Figure 2.2: PEGDA oligomers used as the binder in printed APCP motors. C=C acrylate bonds are severed during polymerization. An increase in C=C bonds indicates higher monomer concentration and therefore reduced binder photopolymerization.

2.3 Sample Preparation

Special Aerospace Services printed the APCP motor used for XPS analysis. The energetic formulation described in Table 2.1 below was prepared for printing. All materials were procured from Sigma-Aldrich.

The Phenylbis(2,4,6-trimethylbenzoyl) Phosphine Oxide photoinitiator used has a maximum UV absorption of 370 *nm*. The photoinitiator is also known as Irgacure 819, or chemical class Bis Acyl Phosphine (BAPO). All components were mixed together in 100 *g* batches. When mixed, the formulation resembled a viscous slurry. The energetic material was shielded from UV radiation until printing.

Table 2.1: Formulation of the APCP motor printed by SAS and used for XPS analysis.

Component	Percent (by mass) of Entire Mixture
Poly(ethylene glycol) diacrylate (Mn \sim 575)	20%
Phenylbis(2,4,6-trimethylbenzoyl) Phosphine Oxide	.7%
Ammonium Perchlorate	64.3%
Aluminum Powder	15%

A Structur3D Printing Discov3ry paste extruder was integrated with a Lulzbot Taz 3 for automated slurry extrusion to the printer build plate. The Discov3ry paste extruder utilizes a positive displacement piston pump with a planetary geared feeder system for high pressure material extrusion. A .80 *mm* nozzle was used during printing, and the system was operated at ambient temperature. The energetic slurry was poured into a syringe, and the syringe was loaded into the Discov3ry paste extruder. Print settings were developed to ensure the syringe chamber pressure remained constant to reduce print defects due to flow rate inconsistencies. As the material was deposited on the print surface, a uvBeast UV flashlight was continuously shown on the extruded material. The flashlight releases 18 *W* of 385-395 *nm* UV radiation, and was positioned approximately 12" normal to the build plate.

Consecutive layer height was set to 1 *mm* to reduce the print time. A UV-curing paste extrusion system similar to the one used in the printing is shown below in Figure 2.3.a. The printed APCP motor used for analysis is shown below in Figure 2.3.b. The motor has an

outer diameter of 30 *mm*, an inner diameter of 10 *mm*, and a height of 7 *mm*. All rectangular samples used for XPS analysis were cut from the top (7th) layer of the same motor shown in Figure 2.3.b.

After printing, the motor was stored for approximately 18 months. After storage, samples used for XPS analysis were cut into rectangular cross sections of approximately 2 *mm* x 2 *mm* x 1 *mm* and attached to the sample holder with carbon tape (as shown in Figure 2.3.c and Figure 2.3.d).

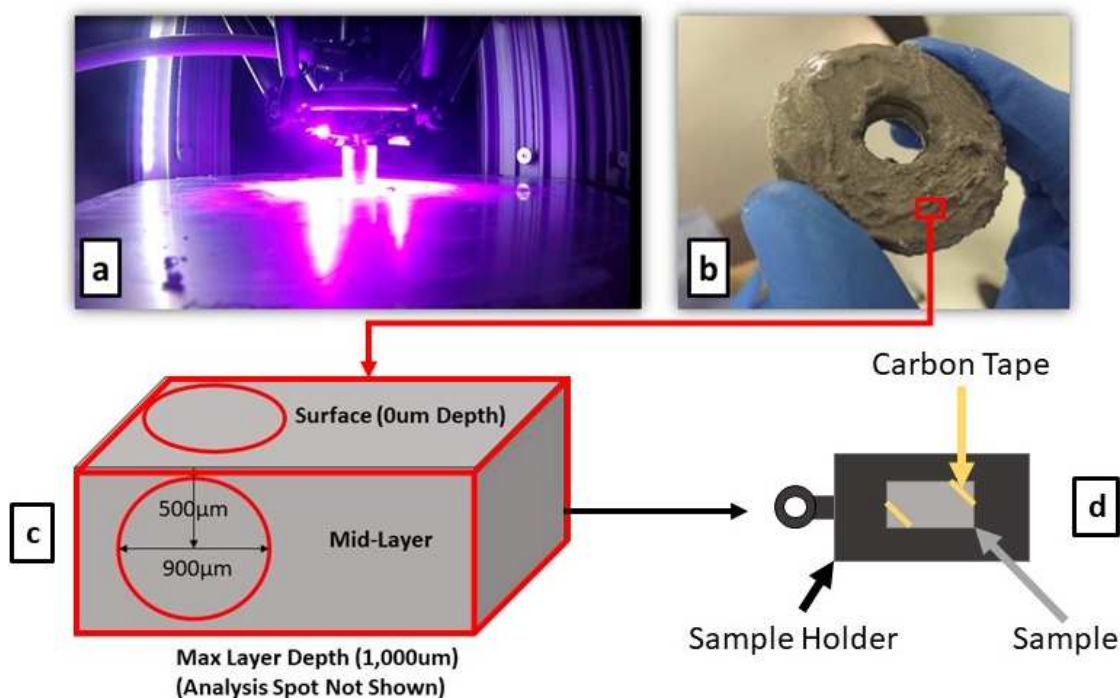


Figure 2.3: 3D-printed APCP SRM sample preparation for XPS analysis. (a) The energetics AM 3D printer used for the development of samples for XPS analysis utilizes a positive displacement piston pump and 385 – 395 *nm* UV lights for in-situ layer curing. (b) All samples used for XPS analysis were prepared from the same printed SRM shown above. Each layer in the printed SRM was 1 *mm*. (c) Samples prepared for XPS analysis were cut into 2 *mm* x 2 *mm* x 1 *mm* blocks. Three different analysis depths were analyzed – surface, mid-layer average polymerization, and 1 *mm*. (d) Rectangular samples were fixed to the XPS sample holder with carbon tape.

Sample preparation is paramount to the success of the experiment. Uneven surfaces may cause “shadowing” of the emission signal because the inclination angle of surface planes is too steep, and the surface does not contribute to electron emission. Mid-layer samples are sliced from the printed SRM and rotated 90° , so the surface roughness is dependent on the cleanliness of the section cut. $1,000\ \mu\text{m}$ samples cleanly delaminate from the previous layer (likely due to insufficient inter-layer polymerization). $0\ \mu\text{m}$ control samples have wavy, uneven surfaces as shown in Figure 2.3.b. The $0\ \mu\text{m}$ depth samples were directly exposed to sunlight for a long enough time to ensure complete binder photopolymerization. Sample positioning in the analysis chamber is not quantifiable, so analysis spot location for mid-layer analysis is estimated, but not exact.

2.4 Experimental Procedure

XPS was performed in a ScientaOmicron HiPP-3 E-XPS using the HiPP III XPS system with ultra-high vacuum analysis chamber. Photoelectrons were generated with monochromatized Al-K alpha X-rays. Pass energy was varied between $100 - 200\ \text{eV}$, and the entrance slit was kept constant at 700 . The entrance aperture was circular at $900\ \mu\text{m}$ diameter. All data was analyzed with CASA XPS software.

Samples fixed on the sample holder were loaded into the XPS system via the fast entry loadlock. Analysis was performed at ambient temperature under ultra high vacuum. The counts per second values for the $0\ \mu\text{m}$ sample are used as the control for all subsequent tests. Sample formulation is constant, laser radiation flux to the control surface is constant, layer

depth is the independent variable in the study, and degree of polymerization is quantified in counts per second and dependent on layer depth. After the control sample was tested, the maximum layer depth analyzed, 1,000 μm , was tested to identify a lower bound DOP. After the upper and lower bound DOPs were established, a mid-layer (500 μm average spot center depth) analysis was run to characterize carbon bond distributions over a 900 μm spot size region centered at a 500 μm layer depth. Subsequent tests were used to refine the data.

2.5 Results

The test results were compared to the C 1s peak spectra binding energies as described in Table 2.2 below [18]. The fit parameters for the data are also described below in Table 2.2. The prominent C-O-C peak seen in all data sets was used as positional calibration of C 1s spectra components in the raw data set.

Table 2.2: CASA XPS data fit parameters for C 1s spectra components.

C 1s Spectra Component	Peak Positional Constraint	Offset from C-O-C Peak	Full Width at Half Max (FWHM) Constraint
C-O-C	286.00 eV +/- .01 eV	0.00 eV	1.78 +/- .05
C=O	289.00 eV +/- .01 eV	3.00 eV	1.20 +/- .05
O-C=O	288.50 eV +/- .01 eV	2.50 eV	2.00 +/- .05
C-C	284.80 eV +/- .01 eV	1.20 eV	1.20 +/- .05
C=C	284.30 eV +/- .01 eV	1.70 eV	1.20 +/- .05

The processed, curve-fit data are shown below in Figure 2.4.

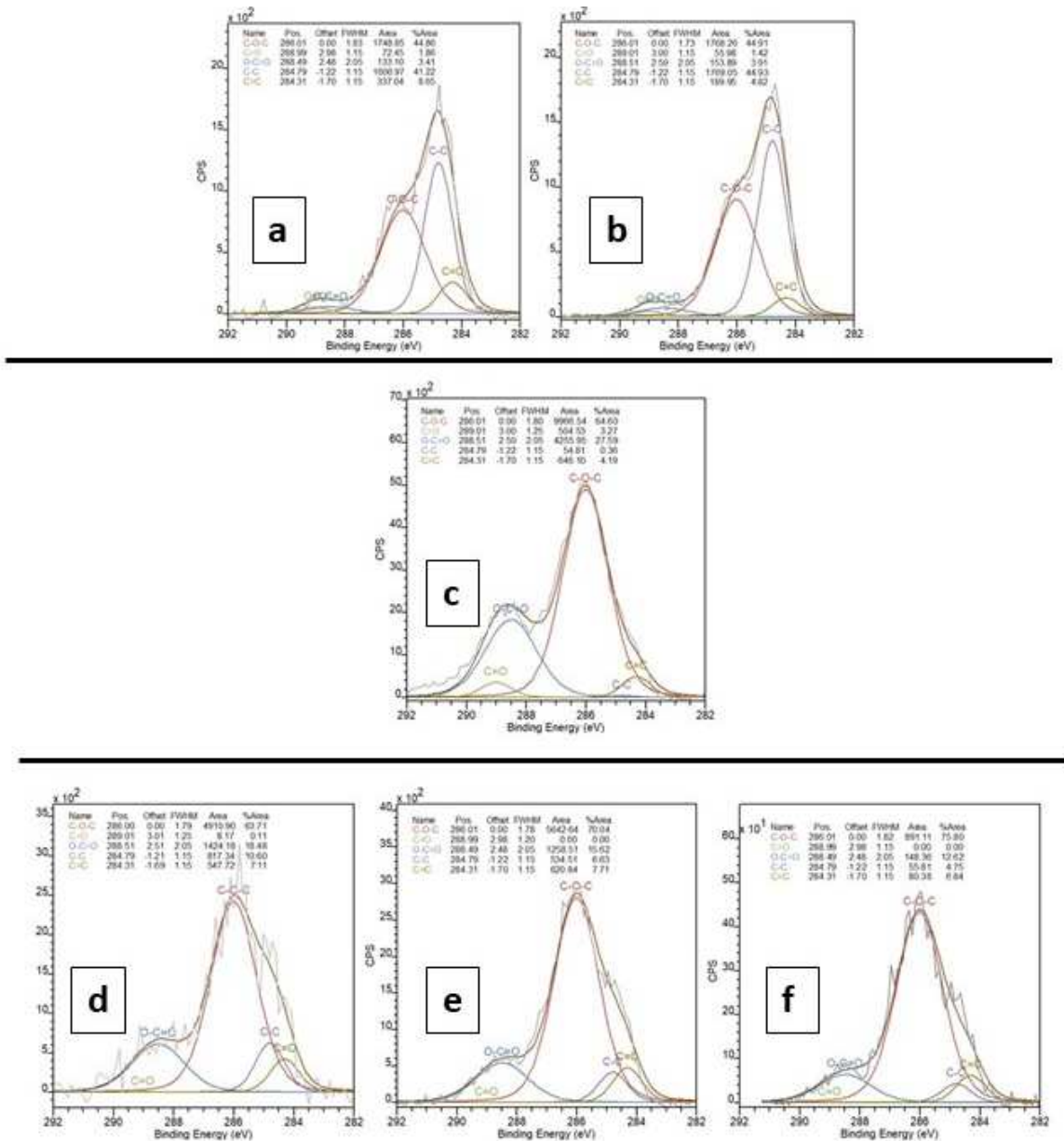


Figure 2.4: Experimental XPS results of C 1s spectra concentrations. Results are shown for control (top two plots a and b), mid-layer (middle plot c), and 1 mm depths (bottom three plots d-f). Curves for C 1s spectra components are fit in the above figure. Results shown in a, b, and f were gathered using a 100 eV pass energy, and results shown in c, d, and e were gathered using a 200 eV pass energy.

2.6 Discussion

The degree of binder photopolymerization is quantified by analyzing the area of C=C peaks in the spectra. An increase in C=C peak area indicates a decrease in polymerization. The C=C peak area was used to quantify polymerization rather than C=C peak percent area because a percent area analysis would introduce more error due to adventitious carbon contamination being incorporated in the calculation. Figure 2.5 shows C=C peak spectra of three data sets: 0 mm, .5 mm, and 1 mm. The relationship between increasing layer depth and increasing C=C peak intensity is clearly shown.

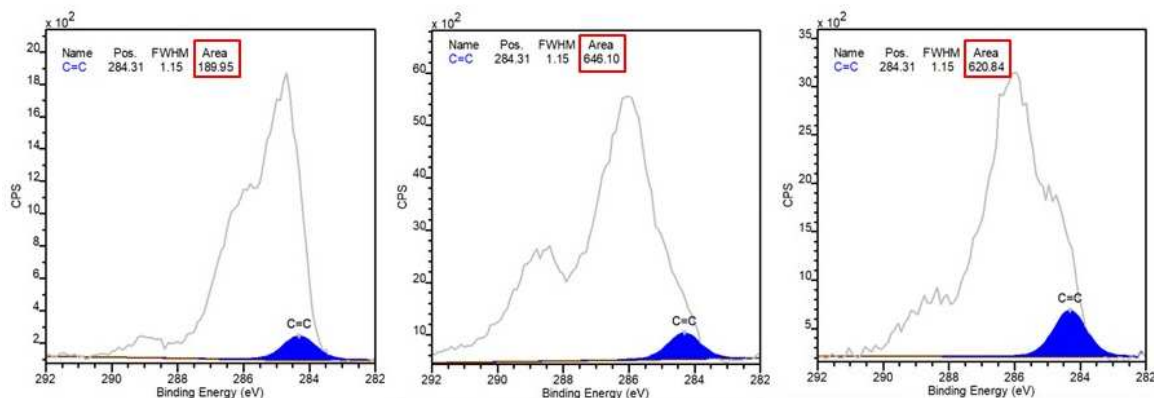


Figure 2.5: Highlighted C=C bond area in curve-fit data for C 1s spectra. From left to right: 0 mm depth, .5 mm mid-layer depth, 1 mm depth. Data from the other 3 tests conducted are not shown.

Adventitious carbon contamination is present in the samples due to the long storage duration. This contamination will be evident in the surface samples as an increase in C-C, C-O-C, and O-C=O bonds. As the analysis depth increases, the adventitious carbon concentration is expected to diminish because contaminants cannot penetrate as deep into the sample. Therefore, the C=C spectra percent area results are skewed for surface analysis data where adventitious carbon contamination increases the total spectra area.

Inconsistencies in spectra intensities between runs may be attributed to sample preparation problems and sample charging. Samples were difficult to prepare and analyze because the composite propellant is heterogeneous and features large oxidizer particulate sizes around

50 μm - 150 μm , concentrations of aluminum powder, and relatively homogeneous concentrations of PEGDA. Because of this heterogeneity, a test may inadvertently record the C 1s spectra of an oxidizer rich region and results may indicate lower than average C 1s bond concentrations relative to other samples with the same layer depth.

The DOP was calculated as the ratio of average C=C peak spectra area of the two control samples to C=C peak spectra areas at a given depth. Since an increase in C=C bond area is indicative of reduced PEGDA monomer concentration, the DOP is defined here as:

$$DOP = \frac{[M_s]}{[M]} \quad (2.1)$$

Where $[M_s]$ is the steady-state monomer concentration at the surface of the material and $[M]$ is the monomer concentration at a given depth l in the material. The monomer concentration is quantified as C=C peak spectra area and is a minimum at the surface of the material. DOP, in equation 2.1 would thus be unity at the surface and gradually decrease, as the monomer concentration increases with depth.

Two models are then considered to define the data set; an exponential decay-based model and a 2nd order polynomial based on experimental data of photopolymerization using a BAPO photoinitiator (Decker, Zahouily, et al., 2001) [19].

In the decay model, the rate of polymerization resulting from photocuring, can be expressed, according to Lee, Prud'homme, et al., 2001 [20] as:

$$\frac{-d[M]}{dt} = R_i + R_p \approx R_p \quad (2.2)$$

Wherein R_i is the rate of free radical initiation and R_p is the rate of polymerization. The rate of polymerization is expressed as [20]:

$$R_p = K_p[M][M^*] \quad (2.3)$$

Wherein $[M^*]$ is the free radical concentration and K_p is a kinetic rate constant. $[M^*]$ depends on the intensity of UV radiation at a given depth, concentration of photoinitiator in the slurry, the quantum yield of the photoinitiation reaction, and the kinetic rate of free

radical generation.

Since the available energy for free radical production at a given depth in the material is a function of UV-wavelength absorbance, differences in bond intensities can be correlated to material absorbance. The intensity of the UV radiation with depth is proportional to the transmittance. The Beer-Lambert law relating transmittance to optical depth of a material is given by:

$$\tau = e^{-\alpha l} \quad (2.4)$$

Wherein α is the attenuation constant, and l is a depth in the material defined as $0 \text{ mm} \leq l \text{ mm} < \infty$. $[M^*]$ is then defined as a function of transmittance by equation 2.5 below [20]:

$$[M^*] = \left(\frac{I_o \tau}{2k}\right)^{\frac{1}{2}} \quad (2.5)$$

Wherein I_o is the initial UV intensity incident to the surface of the material, and k is a constant in this work that contains the concentration of photoinitiator in the slurry, the quantum yield of the photoinitiation reaction, and the kinetic rate of free radical generation. Substituting equations 2.3-2.5 into equation 2.1, integrating, and evaluating over a time t yields:

$$\ln \frac{[M_o]}{[M]} = K_p \left(\frac{I_o \tau}{2k}\right)^{\frac{1}{2}} t \quad (2.6)$$

Wherein $[M_o]$ is the initial monomer concentration at any depth for $t = 0$. Substituting equation 2.4 for the transmittance and assuming t is a constant:

$$\frac{[M_o]}{[M]} = e^{[k_1 e^{\left(\frac{-\alpha l}{2}\right)}]} \quad (2.7)$$

k_1 is a new constant that now incorporates the time constant and k . Applying the boundary condition where at time $t \rightarrow \infty$ the monomer concentration at the surface $[M_{l=0}]$ is equal to $[M_s]$ gives the ratio of initial monomer concentration to the monomer concentration

at the surface at time t :

$$\frac{[M_o]}{[M_s]} = e^{[k_1]} \quad (2.8)$$

DOP is defined at some t as the ratio of monomer concentration at the surface of the material to monomer concentration at a depth l in the material. Therefore, equation 2.7 is divided by equation 2.8 and the theoretical DOP model is given by equation 2.9 below:

$$DOP = e^{[k_1(e^{(-\frac{\alpha l}{2})}-1)]} \quad (2.9)$$

Equation 2.9 is used to predict the theoretical degree of polymerization for comparison to the experimental degree of polymerization results. However, experimental data of acrylate conversion in a photocured coating containing a BAPO photoinitiator follow a different trend [19]. The data show that for $0 \leq l < 40 \mu m$ the degree of polymerization as quantified by acrylate double bond conversion follows a 2^{nd} order decaying polynomial trend.

The decaying polynomial trend may fit a polymerization environment with an excess (saturation) of UV wavelength photons entering at the control surface of the material. If the UV radiation present at a depth in the material exceeds the minimum activation energy (Ea) required to cleave bonds in the photoinitiator, then the DOP at that depth is close to the DOP at the control surface. Once the UV radiation has been attenuated at a depth such that the total radiation present is less than the Ea required for complete free radical production at that depth, the DOP is expected to follow the same decaying exponential trend as the UV radiation. For the samples analyzed in this research, the high material density and absorbance is likely to quickly attenuate UV radiation. The polynomial decay region is likely relatively short in the energetic slurry, and DOP quickly assumes the decaying exponential trend. Data points of the experimental DOP as a function of layer depth are shown in Figure 2.6 below. The DOP model described by equation 2.9 is fit to the experimental data as shown.

Note that the C=C bond area for the third 1 mm depth analysis (shown in Figure 2.4.f) was 80.38 compared to the other two recorded C=C bond areas at 1 mm of 620.84 and

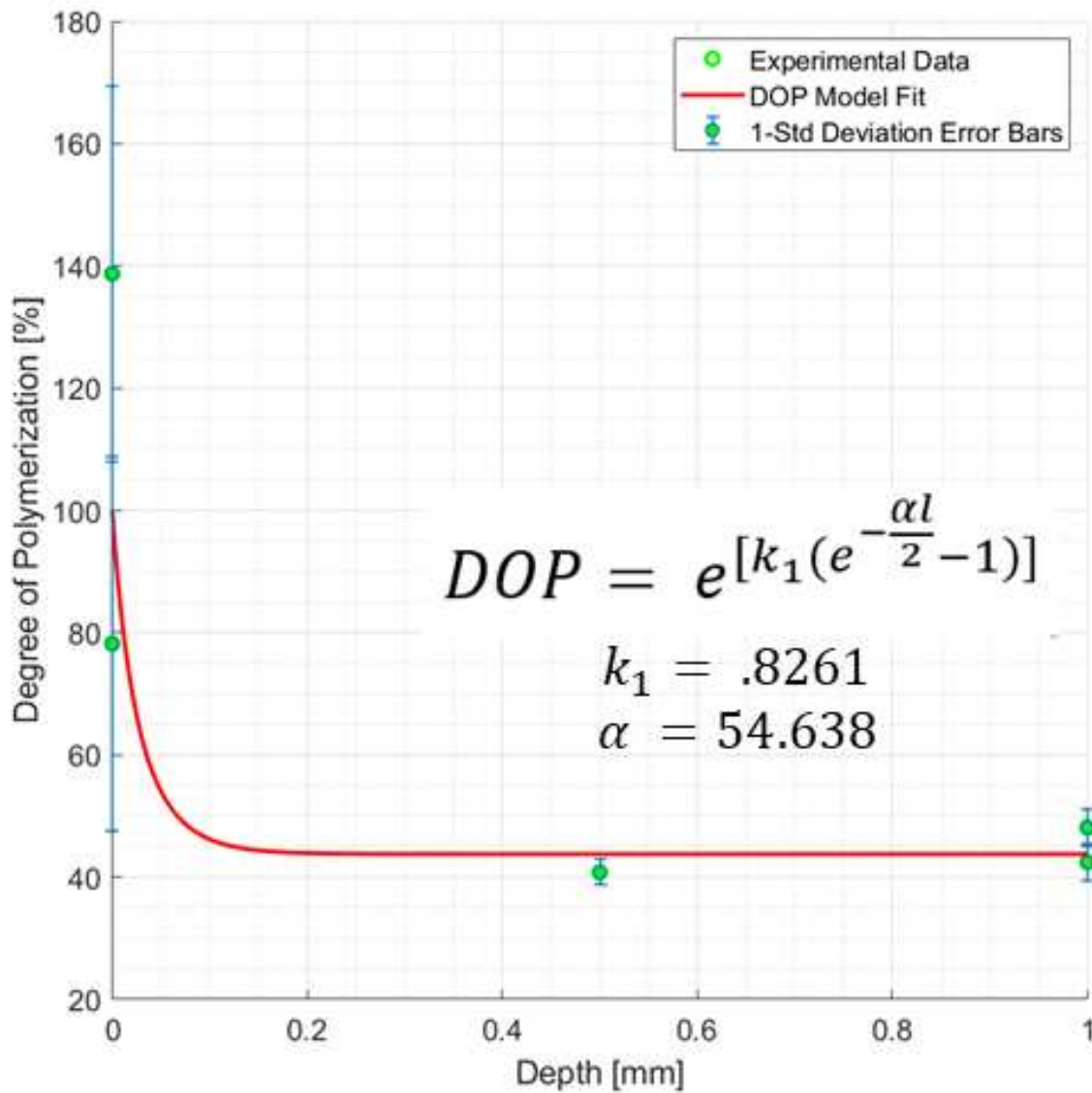


Figure 2.6: Normalized experimental DOP values calculated by equation 2.1. The exponential decay function described by equation 2.9 is fit to the data set for comparison to experimental data. The functions curve fit to the experimental data are normalized to a maximum DOP of 100%. 1-standard deviation error bars are shown at each data point.

547.72. The 80.38 bond area indicates a normalized DOP of 327%; the low bond area at the 1 *mm* depth is an unlikely result compared to the rest of the data set and thus was excluded from the curve fit. The error bars fit to data points at the surface indicate a much higher uncertainty than error bars at the mid-layer or 1 *mm* layer depths. That uncertainty is largely attributed to adventitious carbon buildup and subsequent sample contamination at the surface of samples that is not present at deeper layer depths.

In Figure 2.6 the UV saturation region is close to the surface, and exponential DOP decay begins when the available UV radiation at a depth l drops below the E_a required for complete polymerization at that depth. The transition from UV saturation to exponential decay is expected to occur at depths closer to the surface rather than near the .5 *mm* depth as shown above. However, the UV radiation dosed to the surface of the material will dictate when the DOP transitions from polynomial to exponential decay; a higher dose would create a larger excess of photons at the surface and transition to the exponential decay region would occur at a deeper layer depth.

It appears that the exponential decay model fits the experimental data best, however, no data is available for small layer depths between $0 < l < .5$ *mm* where the transition from UV saturation to exponential decay is likely to occur. The low separation in binding energies for C-C and C=C bonds, .5 *eV*, also reduces the confidence in the interpreted results and model fit. Adventitious carbon overlap into the 284.3 *eV* C=C bond region may have contributed to error in the analysis. Furthermore, a total of 6 data points has been collected, and the 3rd data point in the 1 *mm* depth test was determined to be an outlier in the scope of the data. Many more tests are needed to improve the confidence of the analysis, and to determine the transition from UV saturation to exponential DOP decay in the material.

Error in the data set can be partly attributed to flaws in the experimental procedure. Most notably, the curve fit models assume a mid-layer analysis is run at a constant .5 *mm* depth, but an inability to prepare samples at a constant .5 *mm* layer height necessitated that an average polymerization analysis of the side of a sample be run.

Also important in the results analysis is the importance of available oxygen content at analysis layer depths. Since an increased polymer cross-linking density will restrict oxygen diffusion rate [21], free-radical photopolymerization processes that are restricted due to oxygen inhibition may propagate further at deeper layer depths with lower oxygen content [22]. These effects may contribute to changes in the UV intensity attenuation relationship described in equation 2.5 and model deviances at various layer depths.

2.7 XPS Conclusions

The data have shown relationships between carbon 1s bond concentrations at different analysis depths. Increases in C=C bond intensity are indicative of reduced PEGDA polymerization. The decay of UV intensity with increasing sample depth is captured by C 1s spectra, but flaws in sample preparation, adventitious carbon build up, and overlapping C-C and C=C peaks currently limit the validity of the radiation absorption-based models. A more controlled sample preparation and storage environment is essential for refining the model for future predictions of DOP as a function of printed layer height.

Other methods of acrylate bond quantification may be considered as well. Fourier-transform infrared spectroscopy or spatially resolved spectroscopy may be better suited than XPS to analyze C=C double bonds [23]. It is anticipated that a robust understanding of binder photopolymerization processes will become increasingly important as the emerging field of energetic materials AM progresses.

The DOP results found in this chapter are especially important in interpreting the XCT results in chapter 3. The porosity data described in the following chapter are validated by the DOP gradient found along the build direction.

CHAPTER 3

X-RAY COMPUTED TOMOGRAPHY ANALYSIS OF 3D-PRINTED SRM SAMPLES

The purpose of this chapter is to analyze porosity defects inherent in 3D-printed APCP SRMs. The results gathered from XCT scans of printed samples are interpreted and porosity defect mechanisms unique to AM are presented. The large polymerization gradients seen in samples indicate that inter-layer adhesion is poor and that polymer mobility is higher at deeper layer depths where polymerization is low. It is hypothesized that insufficient binder polymerization is the primary cause of porosity in 3D-printed APCP. The primary objective of this chapter is to quantify porosity in the build direction and correlate the results to the XPS data. Implications of the porosity data gathered in this chapter on propellant deflagration are considered later in subsection 4.4.

3.1 XCT Overview

The second method of NDE utilized in this research for analyzing 3D-printed SRM samples is XCT. This method was chosen because of its ability to image the internal mesostructure and microstructure of SRMs. As previously described in chapter 2, DOP decreases exponentially with layer depth. Additionally, oxygen present at a photoinitiated section of material will terminate cross-linking chains and inhibit further polymerization. Polymerization inhibition is particularly important at the interface between the top of a deposited layer of propellant and the bottom layer of propellant deposited on top of the previous layer. Sequential layer adhesion at this interface is poor in the APCP SRM samples printed and analyzed in this research because of both the oxygen-driven chain termination at the surface of the previous layer and because of minimal photoinitiation at the bottom of the 1 *mm* build layers.

It is hypothesized that this weak layer adhesion increases porosity at the two-layer interface and thus creates sequential localized porosity gradients in printed APCP samples. The

hypothesized sequential meso/microscale porosity defects caused by inter-layer delamination are illustrated below in Figure 3.1.

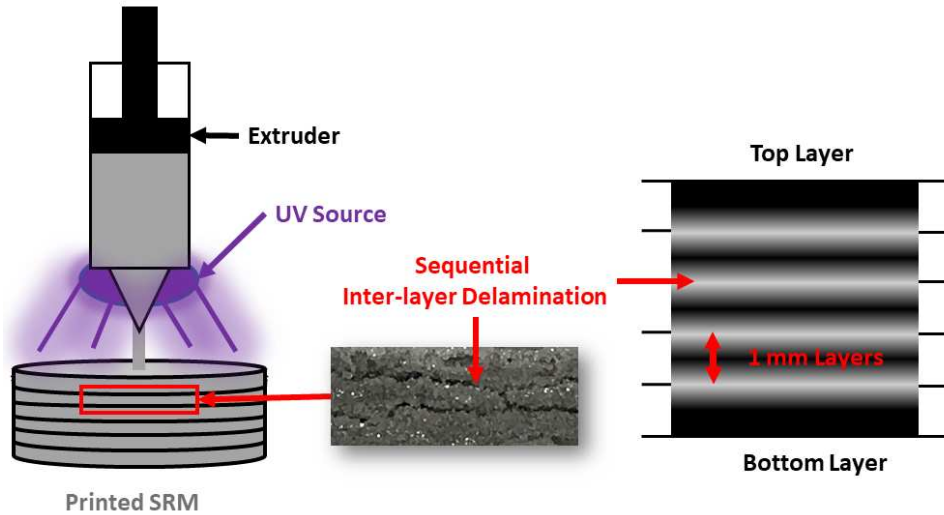


Figure 3.1: Hypothesized sequential porosity defects in 3D-printed APCP SRMs attributed to inter-layer delamination.

XCT was used to analyze and quantify this suspected sequential porosity inherent in printed samples. Understanding porosity defects inherent in the manufacturing process is crucial in predicting how a propellant will perform during deflagration. The results from this XCT analysis are considered later in subsection 4.4 for modeling porosity-graded propellants.

3.2 Sample Preparation and Experimental Procedure

Similar to the XPS analysis sample preparation, small samples for XCT analysis were cut from a 3D-printed APCP SRM. The sample preparation procedure is shown below in Figure 3.2.

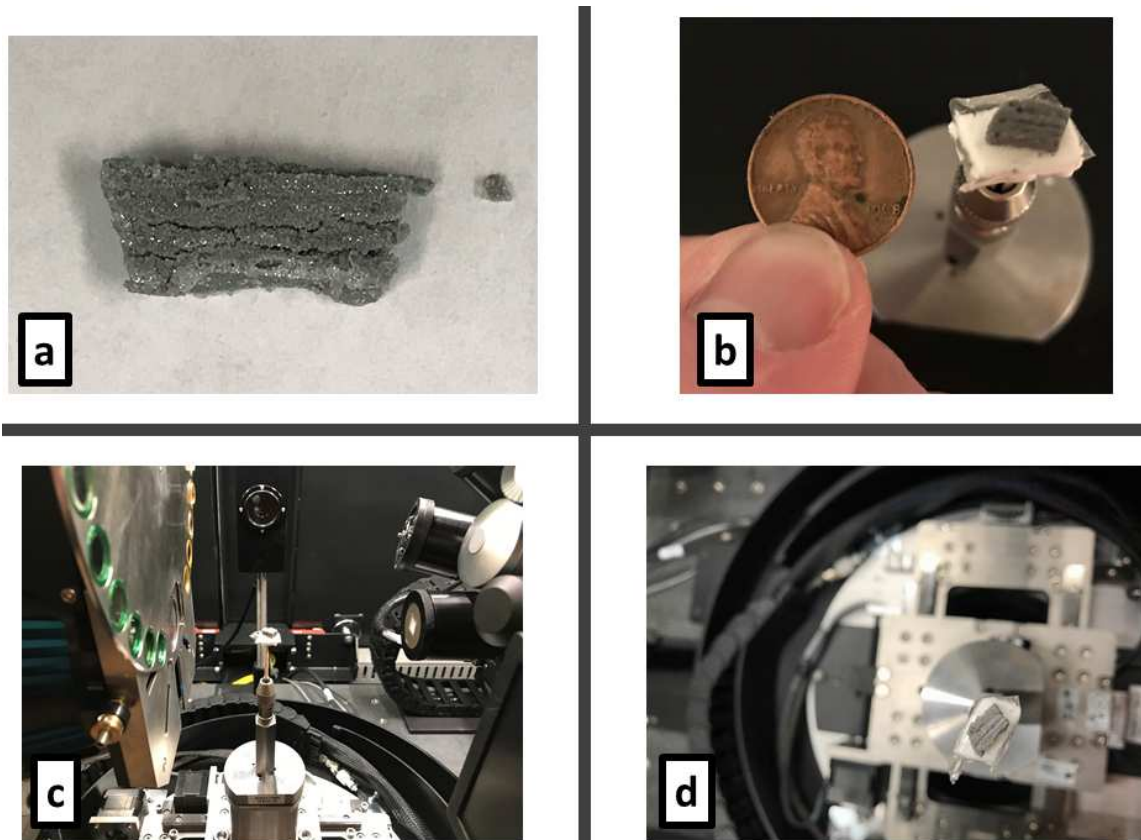


Figure 3.2: Printed APCP SRM sample preparation for XCT analysis. (a) A sample is cut from the same 3D-printed SRM used for XPS analysis. Sequential layer adhesion quality is noticeably poor because little or no photopolymerization occurs at 1 *mm* layer depths. (b) The cut sample is mounted on a sample holder (the sample analyzed in run 2 is shown). The sample shown is approximately 4 *mm* x 3 *mm* x 2 *mm*. The sample and reference coin are at approximately equal depth perspectives. (c) The sample holder is loaded into the Zeiss Versa 520 micro-CT x-ray microscope. The x-ray source is shown (left) and detector is shown (right). (d) An overhead view of the sample in the machine is shown.

Sample analysis parameters for each of the two scans are described below in Table 3.1.

Table 3.1: XCT analysis settings

Scan	Objective Lens	X-ray Voltage	Power	Exposure Time	Pixel Size
021419	0.4X	60 kV	5 W	20 s	3.2344 μm
031219	4.0X	80 kV	7 W	20 s	5.4991 μm

3.3 Results

A total of two scans were performed to capture porosity trends in successive layers of 3D-printed APCP SRM samples. A full XCT image of scan 031219 and a cross-sectional planar view is shown below in Figure 3.3. The white glow on the top of the sample in the image is due to beam hardening effects from the x-rays. The images shown have been processed to filter out low contrast materials (sample mounting foam, toothpick, tape). The PEGDA binder in the composite matrix is shown as dark grey, the ammonium perchlorate is light grey, and the relatively higher-impedance aluminum powder appears white. Porous regions in Figure 3.3 are highlighted in red.

Dragonfly ORS was used to gather porosity data for both scans. The method for quantifying sample porosity was inherently subjective. Since the samples analyzed did not fill the entire XCT scan volume region, part of the scan images include data for unoccupied space around the samples. This unoccupied space cannot be filtered out from the data set because the air present inside the samples in porous regions would also be filtered out. Additionally, the data set could not include the unoccupied space surrounding the sample because the calculated sample porosity would be inflated. To address these problems scans 021419 and 031219 were cropped into orthorhombic volumes with approximate dimensions 1 *mm* x 1 *mm* x 2.8 *mm* and 1 *mm* x 1 *mm* x 3.8 *mm*, respectively. The locations of the cropped volumes in the data sets were chosen to capture clear layer separation and minimal porosity. Regions in the material where excessive layer delamination was present were not captured

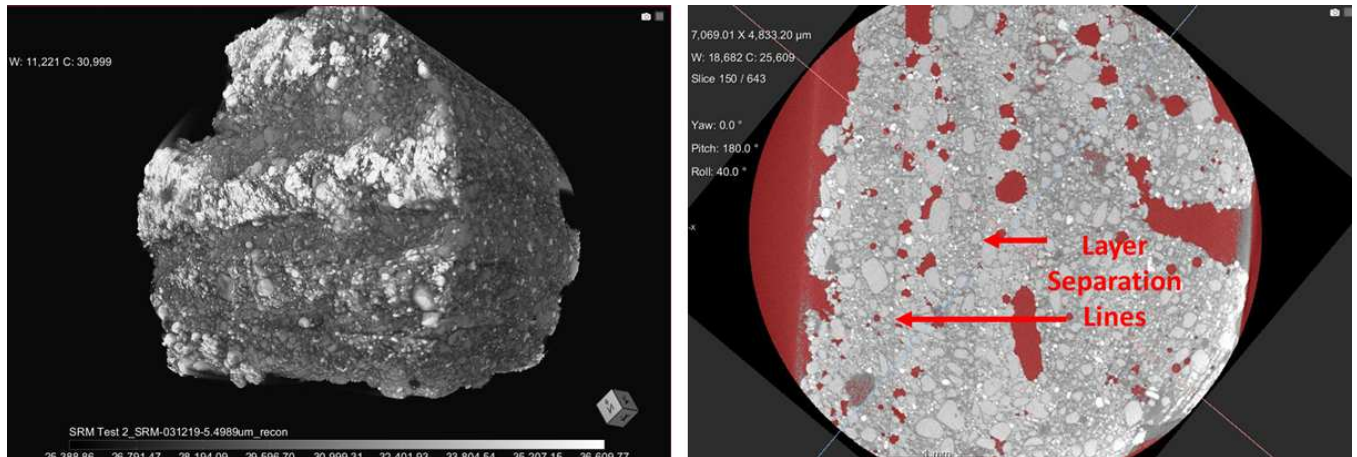


Figure 3.3: XCT image of 3D-printed APCP SRM sample and cross-sectional plane. The entire APCP sample analyzed in scan 031219 is shown (left). Layer separation lines of a cross-sectional plane in scan 031219 are indicated (right). Porous regions are highlighted in red.

in the porosity calculations to avoid skewing the data set.

After the data sets were cropped, cross-sectional planes were aligned for histographic segmentation analysis in Dragonfly ORS. Because the orientation of the samples relative to the data processing coordinate frames was unknown, visual alignment of planes parallel and normal to the SRM build direction was required. Plane alignment in Dragonfly ORS is shown below in Figure 3.4.

This visual planar alignment method represents the second source of subjective systematic error present in the data analysis.

After the histographic segmentation plane was aligned normal to the build direction, layers were segmented in Dragonfly ORS to give spatial data of porosity and binder constituents in the samples. Data sets for scans 021419 and 031219 were collected at planar separation distances of $3.30 \mu m$ and $5.50 \mu m$, respectively. The average densities of scans 021419 and 031219 were found to be 87.64% and 92.26%, respectively. Planar porosity concentration data sampled normal to the build direction are plotted below in Figure 3.5.

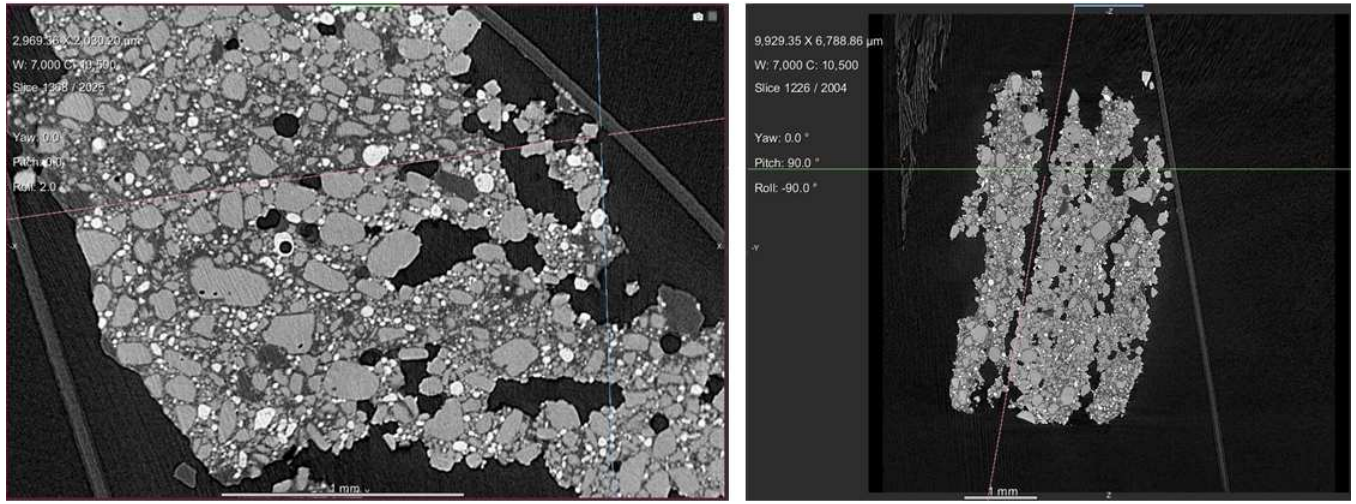


Figure 3.4: Plane alignment procedure for histographic segmentation of samples. Both images show plane alignment for scan 021419. The pink line represents a plane normal to the image and aligned parallel to the perceived build direction (left). A second planar view (orthogonal to the image on the left) is used to verify that the pink plane is parallel to the build direction (right).

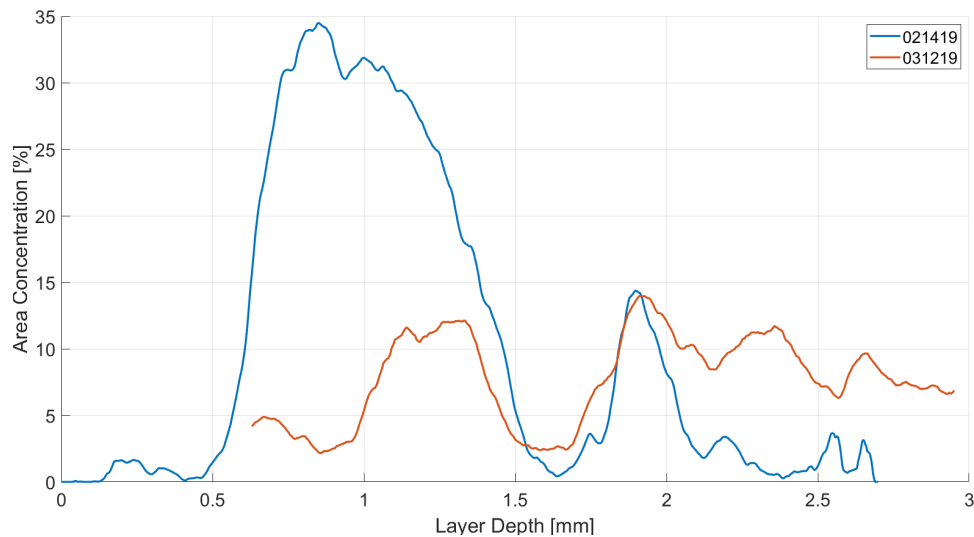


Figure 3.5: Porosity data for 3D-printed APCP SRM scans 021419 and 031219. Approximately 2.7 mm and 2.5 mm of the data sets were cropped in the build directions for samples 021419 and 031219, respectively.

3.4 Discussion

From Figure 3.5 it appears that some amount of periodicity in porosity along the build direction may be present for both scans. Peak amplitudes are similar for both scans with the exception of the first period in scan 021419. The periodicity between the first two peaks in both scans appears similar as well; the sharp reductions in porosity concentrations indicative of layer separation in both scans at the first peaks are approximately $100\ \mu\text{m}$ apart when the second porosity peaks are aligned. Periodicity for both scans appears to be aligned around $700\ \mu\text{m}$. The large period and amplitude of peak one in scan 021419 are outliers in the data sets likely a result of delamination during sample preparation. Binder concentration was found to be periodic in the build direction as well, as shown in Figure 3.6.

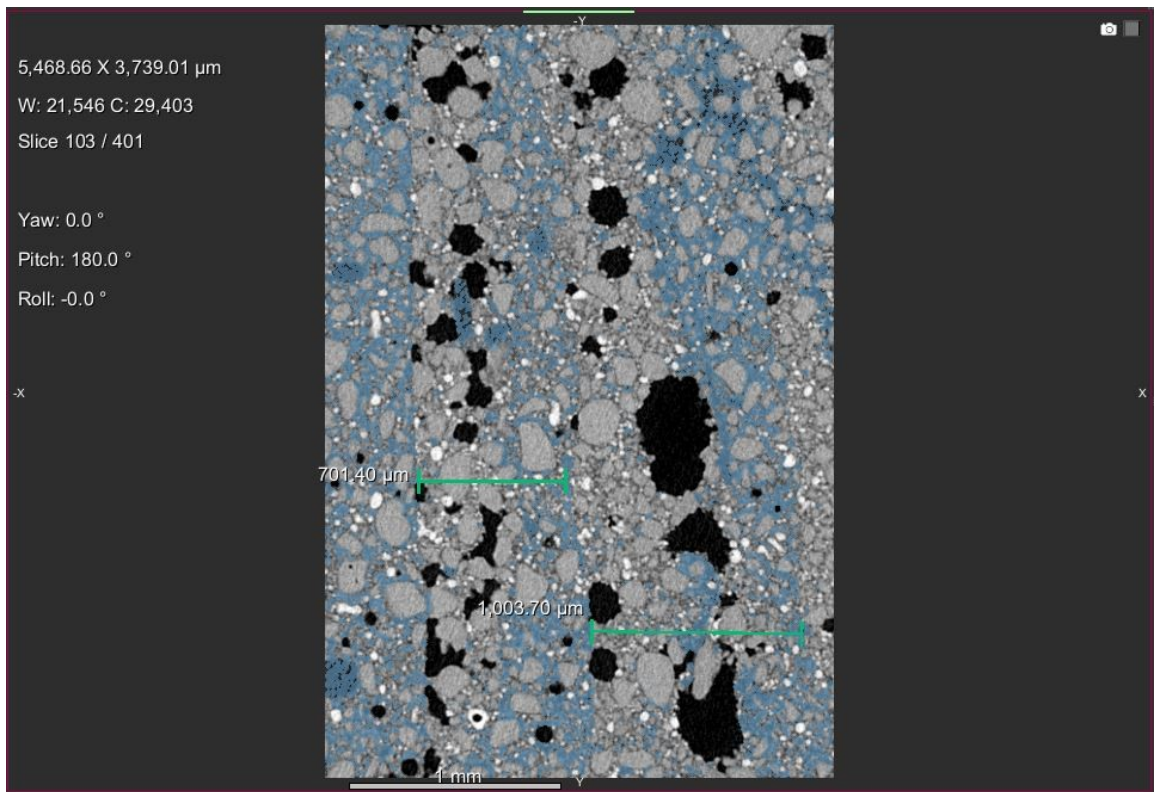


Figure 3.6: Highlighted PEGDA binder in a cross-sectional plane parallel to the build direction in sample 031219. Regions highlighted in blue indicate binder-rich areas.

The results shown in Figure 3.6 are indicative of binder phase separation from the solid aluminum and ammonium perchlorate particulates via high interfacial energy. In a composite propellant with excellent wetting properties, the continuous phase (binder) will wet to the solid particulates and form a homogeneous material after curing. In contrast, the blue stripes shown in Figure 3.6 indicate that significant phase separation has occurred.

Binder concentration regions shown in Figure 3.6 help to explain why porosity in scans appears to be periodic. Binder-rich regions appear to be concentrated in areas about $300\ \mu\text{m}$ into new layers, and the first $300\ \mu\text{m}$ of layers appears to be more porous than the binder-rich region. Therefore, the binder is phase-separating near the surface of the material and migrating downwards in the layer, leaving behind porous regions near the surface of the material. The surfaces of layers should theoretically have binder concentrations close to 20% (by mass) because binder photopolymerization at the surface will inhibit polymer mobility and prevent phase separation. However, since UV radiation decays exponentially through the material (see chapter 2), most of a deposited layer is un-polymerized and maintains mobility for phase separation.

The relationship between porosity and binder concentration is shown below in Figure 3.7. Layer separation lines in Figure 3.7 should be evident where there are discontinuities in binder concentrations from high to low values; $1\ \text{mm}$ separation lines are shown in the figure and aligned at the suspected layer change at $1.80\ \text{mm}$. The binder concentration shown is termed "TMD Relative Binder" because it is calculated as the ratio of binder constituent image voxels to total voxels of APCP; porosity voxels were removed from the total APCP voxel summation.

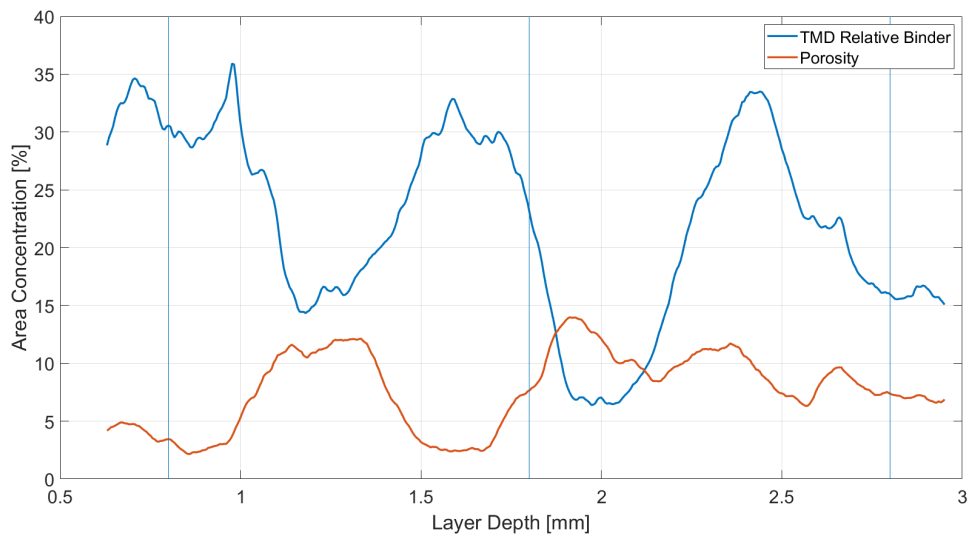


Figure 3.7: Porosity and binder concentration data from XCT scan 031219. 1 mm layer separation marks are shown as vertical blue lines. Minima in binder concentrations coincide with porosity maxima, indicating binder phase separation contributes to graded-porosity in samples.

Although the original APCP SRM 3D-printed and used for analysis was intended to be printed with 1 mm layer heights, it appears that layers were not uniform. The 1 mm layer segmentation lines shown in Figure 3.7 do not coincide with the porosity and binder peaks. The lack of uniformity in layer heights is also seen previously in Figure 3.6; XCT scan data indicated layer depths between 700 μm and 1,000 μm . This difference in layer depths was likely attributed to insufficient structural integrity of the samples due to minimal binder photopolymerization below the surface and layer deformation during sample preparation.

3.5 XCT Conclusions

The initial hypothesis that layer delamination in samples was responsible for meso/microscale porosity defects was found to be only partly true; a second mode of porosity generation was found to exist in samples as a result of binder phase separation from solid phase constituents in the composite propellant matrix. However, complete binder photopolymerization may eliminate both porosity defect modes because layers would adhere to each other and complete polymerization inhibits binder movement in the composite propellant matrix.

Complete polymerization may be difficult to attain in practice; oxygen content near the surface of the material may terminate free-radical cross-linking reactions, reducing inter-layer adhesion [22] as previously discussed in subsection 2.6. It is also important to consider the limits of XCT analysis on quantifying sample porosity. The minimum feature sizes identified in scans 021419 and 031219 were $3.2344 \mu m$ and $5.4991 \mu m$, respectively. Porosity features in the printed samples smaller than these pixel sizes could not be resolved. XCT is a capable tool for analyzing features near mesoscale resolution in composite materials, but it lacks the resolution needed for analyzing smaller microstructure features.

The binder and porosity gradients seen in the XCT data highlight the importance of more complete binder photopolymerization during the printing process. The high density anisotropy seen in the samples creates variable burn rates which may cause undesirable material behavior. Binder gradients caused by polymer phase separation would cause fluctuations in burn rate as the flame front moves through oxidizer-rich and fuel-rich regions, but localized regions of exceptionally high porosity may cause dangerous increases in burn rate in confined locations. The effects of graded-porosity defects on propellant defect are modeled later in subsection 4.4.

CHAPTER 4

NUMERICAL MODELING OF POROSITY-GRADED 3D-PRINTED SRMS

The XPS data in chapter 2 were used to validate the presence of periodic propellant density anisotropy in the grain build direction seen in chapter 3. The objective of this chapter is to use the experimental XCT porosity data to predict the impact of propellant defects generated during printing. These results are the basis for future research seeking to develop printed tailored energetic materials with intentionally porous internal structures for deflagration manipulation.

4.1 Propellant Deflagration Modeling in ANSYS Autodyn

This research seeks to model the predicted transient pressure profile of additive-manufactured SRMs using ANSYS Autodyn Computational Fluid Dynamics (CFD) software. This modeling approach is similar to traditional HE modeling in that the transport equations governing mass, momentum, and energy transfer describe inviscid compressible fluids. However, in contrast to HEs, propellant deflagration is initiated when a burning front contacts a section of material, rather than a pressure front. This burning front travels behind the pressure front and at orders of magnitude lower velocities.

The governing equations for conservation of mass, momentum, and energy in Autodyn are the Euler equations for compressible fluid flow. The Euler equations differ from Navier-Stokes equations in that the flow is assumed to be inviscid, so diffusive transport effects on conserved properties is ignored. Therefore, propellant deflagration is only initiated by the convective burning front and not influenced by thermal conduction. The Euler equation for conservation of energy in compressible flow relates internal energy to kinetic energy as shown below in equation 4.1.

$$E = \rho e_g + \frac{1}{2} \rho u^2 \quad (4.1)$$

Wherein E is the total energy of the system, ρ is the density of mass in the system, and u is the velocity of the mass in the system. The first term of the equation, ρe_g , describes the internal energy of the system, and the second term describes the kinetic energy of the system.

Because of the differences in reaction ignition mechanisms between deflagrating propellants and HE's, an Equation of State (EOS) is needed to couple changes in internal energy to state variables such as pressure. Equations of state are commonly used in applications to relate thermodynamic properties to state variables such as pressure and volume. A commonly used EOS in engineering applications is the ideal gas law. Recent efforts to model propellants in Autodyn have focused on incorporating the slow powder burn (beta) EOS to describe material deflagration. The slow powder burn EOS incorporates user-input experimental data and thereby eliminates the need to model combustion kinetics and first principles. This multi-phase model (Atwood, Friis, Moxnes, 2003) considers combustion in individual cells composed of a volume of solid and gaseous phase propellant [24]. As the solid phase combusts into gaseous phase, the volume of the Euler cell remains constant, but the density in the cell approaches the density of the gaseous phase. A visual representation of a unit cell of material considered in the model is shown below in Figure 4.1.

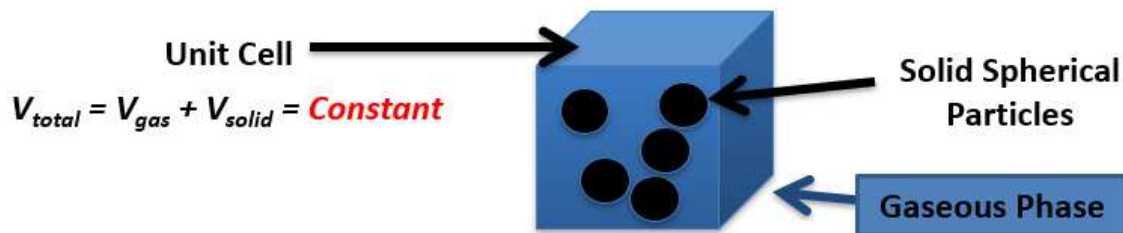


Figure 4.1: Visual representation of unit cell volume composed of solid and gaseous propellant.

Heat conduction between the solid phase and gaseous phase in the numerical cell volume is ignored in the model. In addition, temperature is ignored in both the solid phase linear EOS and slow powder burn EOS. As combustion in the cell occurs, the internal energy of the

propellant, e_g , is converted to kinetic energy as described in equation 4.1. Since temperature is ignored, no thermal energy is created and all of the internal energy is converted directly to kinetic energy. Since mass must be conserved, the density of multi-phase propellant material in a single Euler cell must be fixed such that:

$$\rho(t) = \frac{M_s(t) + M_g(t)}{V} \quad (4.2)$$

Wherein $\rho(t)$ is the density of the cell in time, $M_s(t)$ is the mass of solid propellant particles in the cell, $M_g(t)$ is the mass of gaseous phase in the cell, and V is the volume of the cell. The model considers both the change in average phase density during combustion and compaction effects on solid phase density. If there are initially no pores in the propellant and no gaseous phase, the density of material in the cell is given as:

$$\rho(t) = \rho(t_o) = \bar{\rho}_s(t_o) \quad (4.3)$$

Wherein $\rho(t_o)$ is the initial density of the cell and $\bar{\rho}_s(t_o)$ is the average initial density of solid phase in the total cell volume. As seen in equations 4.2 and 4.3 if no gaseous phase exists in the cell, $\rho(t)$ will be constant and combustion will not begin. Although there is a TMD defined for the propellant solid phase ($\rho_s(t)$), the initial solid phase density $\bar{\rho}_s(t_o)$ will be below TMD and convective burning will occur. The implications of propellant density on burn rate will be discussed in detail later in subsection 4.4. Figure 4.2 shows how the different densities considered in the slow powder burn model change during combustion.

In Figure 4.2 $\rho_g(t)$ is the density of the gaseous phase in the cell and $\bar{\rho}_g(t)$ is the average density of gaseous phase in the total cell volume. This figure illustrates the compressibility of the gaseous phase because $\rho_g(t)$ initially increases much more rapidly than $\bar{\rho}_g(t)$. During combustion $\bar{\rho}_g(t)$ increases inversely proportional to $\bar{\rho}_s(t)$ since mass in a cell is conserved and all solid mass must be converted to gaseous phase mass. In contrast, $\rho_g(t)$ is calculated as the ratio of gaseous phase mass to gaseous phase volume in a cell, so regions where $\rho_g(t) > \bar{\rho}_g(t)$ indicate the gaseous phase is being compressed by the solid phase. As combustion proceeds, gas generation increases the gas pressure, the gaseous phase expands in the cell,

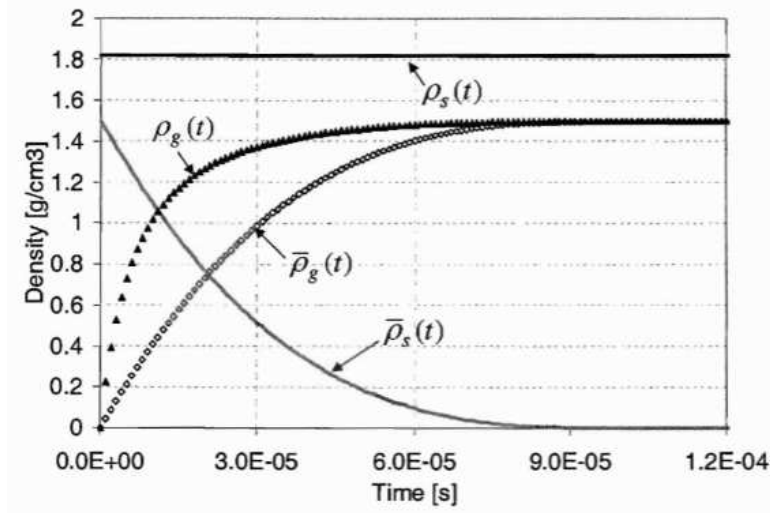


Figure 4.2: Analytical calculation by Atwood displaying density changes of phases during combustion.

and the rate of increase in gaseous phase density ρ_g decreases.

Upon ignition of a single cell of material, the reaction rate \dot{F} proceeds as defined by equation 4.4 below.

$$\dot{F} = G(1 - \alpha F)^{c_g} \dot{b}(P_g) \quad (4.4)$$

Wherein G , c_g , and α are geometric constants and F is the reaction ratio. F is defined in equation 4.5 below.

$$F = \frac{M_s(t_0) - M_s(t)}{M_s(t_0)} \quad (4.5)$$

Wherein $M_s(t_0)$ is the initial solid mass in a cell and $M_s(t)$ is the solid mass in a cell at a time t . The reaction ratio is inversely proportional to $\bar{\rho}_s(t)$, indicating that combustion of a single cell of material nears completion as F approaches unity.

Atwood then describes the slow powder burn EOS for gaseous phase as:

$$P_g = n' RT_g \rho_g(t) \text{Exp}\left(\frac{\rho_g(t)}{\rho_{g,max}}\right) \quad (4.6)$$

Wherein n' is the molar mass, R is the ideal gas constant, T_g is the temperature of the gas, and $\rho_{g,max}$ is the maximum density of the gas. The internal energy is defined as $n' RT_g$

and the volume specific internal energy is defined as $e_g \rho_g$.

4.2 Modeling homogeneous APCP propellant with variable burn rate

As a first step in modeling 3D-printed APCP SRMs, experimental data for a user-defined APCP material was input to Autodyn. The slow powder burn EOS requires material data for pressure and corresponding burn rate. The data used were gathered by Lengelle for a series of closed-bomb tests [25]. The APCP used in the closed-bomb tests is composed of 18% aluminum, 50% AP (100 μm), 18% AP (10 μm), and 14% HTPB binder. The data are described below in Table 4.1.

Table 4.1: Experimental APCP burn rate and pressure data

P_g [kPa]	\dot{b} [$\frac{m}{s}$]
2.20x10 ²	.0024
3.30x10 ²	.0030
5.00x10 ²	.0032
1.00x10 ³	.0052
1.40x10 ³	.0061
2.00x10 ³	.0071
3.00x10 ³	.0085
4.00x10 ³	.0094
6.00x10 ³	.0110
8.00x10 ³	.0130

The burn rate and pressure relationship data were only listed to 8 MPa to avoid modeling APCP propellant above the critical pressure where the pressure exponent increases above 1 [26]. The Vielle’s law expression utilized in the slow powder burn model describes the relationship between burn rate and pressure and includes a constant c that defines the burn rate when $P_g = 0$:

$$\dot{b} = aP_g^n + c \quad (4.7)$$

Wherein a is the constant of proportionality, n is the burning rate pressure exponent, and c is the added constant.

To ensure that the data input to Autodyn are indicative of a single composite propellant test and not a series of individual closed-bomb tests, Vielle's law constants were matched to the data set. If the data were not fit to a single Vielle's law curve, the propellant would burn erratically because the experimental burn rate and pressure data do not exactly follow a single burn rate and pressure relationship. The least-squares fit procedure used in this research for the APCP data set is similar to the one used by Smestad [27]. Equation 4.8 describes the fit for the pressure exponent, n .

$$\sum_{i=1}^N P_i^n \ln P_i \left(\left(NP_i^n - \sum_{j=1}^N P_j^n \right) \frac{\sum_{j=1}^N P_j^n (N\dot{b}_j - \sum_{k=1}^N \dot{b}_k)}{\sum_{j=1}^N P_j^n (NP_j^n - \sum_{k=1}^N P_k^n)} - \left(N\dot{b}_i - \sum_{j=1}^N \dot{b}_j \right) \right) = 0 \quad (4.8)$$

After the pressure exponent has been fit, a constant c is fit to the data set. c is not traditionally included in Vielle's law for burn rate calculation, however the constant is added to prevent a zero burn rate condition at zero pressure. A zero gas pressure condition exists in the model at the time of ignition because no gaseous phase is present, so according to equation 4.6 no gas pressure exists. This would be problematic for the model because zero gas pressure and zero burn rate would result in a zero reaction rate and combustion would never proceed. The least-squares fit equation for c is described below in equation 4.9.

$$c = \frac{1}{N} \sum_{i=1}^N \left(\dot{b}_i - P_i^n \frac{\sum_{j=1}^N P_j^n (N\dot{b}_j - \sum_{k=1}^N \dot{b}_k)}{\sum_{j=1}^N P_j^n (NP_j^n - \sum_{k=1}^N P_k^n)} \right) \quad (4.9)$$

The constant of proportionality a is fit to the experimental data set as described below in equation 4.10.

$$a = \frac{\sum_{i=1}^N P_i^n (N\dot{b}_i - \sum_{j=1}^N \dot{b}_j)}{\sum_{i=1}^N P_i^n (NP_i^n - \sum_{j=1}^N P_j^n)} \quad (4.10)$$

The experimental APCP data set and least-squares fit results are shown in Figure 4.3.

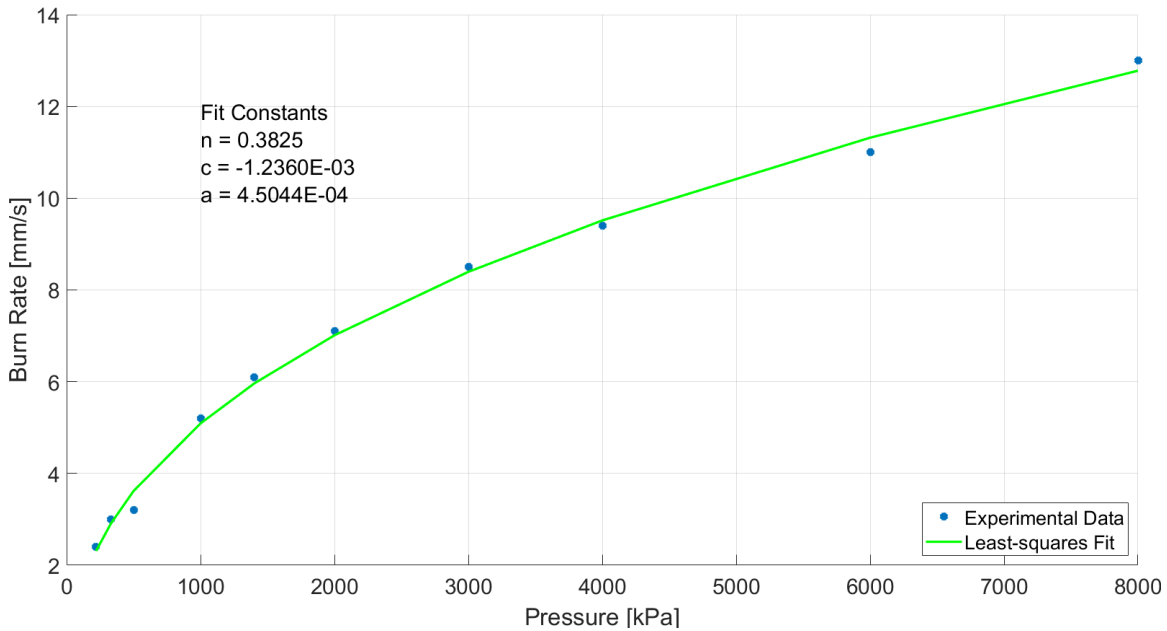


Figure 4.3: Least-squares fit of Vieille’s law constants for experimental APCP closed-bomb burning test data.

Note that the c constant added to Vieille’s law was fit as a negative value. Mathematically, a negative c would result in negative burn rate when $P_g = 0$. Although a propellant cannot physically have a negative burn rate, a \dot{b} less than zero at low pressure indicates that the propellant will not sustain combustion. Autodyn will allow negative burn rate values for a single cell, but it will not allow negative reaction rates; if ignition of a cell occurs the cell will sustain combustion regardless of pressure. Negative reaction rates that exist when P_g is near 0 are automatically increased to some value just above 0 to allow the reaction to proceed.

A final data set is calculated using the results from equations 4.8 - 4.10. The data set is shown below in Table 4.2

The constants calculated from equations 4.8 - 4.10 are not explicitly defined anywhere in the slow powder burn EOS, they are instead implicitly defined by the tabulated P_g and \dot{b} values in Table 4.2 above.

Table 4.2: Least-squares fit APCP burn rate and pressure data input to Autodyn slow powder burn EOS

P_g [kPa]	\dot{b} [$\frac{m}{s}$]
1.00×10^2	.0014
1.00×10^3	.0051
2.00×10^3	.0070
3.00×10^3	.0084
4.00×10^3	.0095
5.00×10^3	.0105
6.00×10^3	.0113
7.00×10^3	.0121
8.00×10^3	.0128
9.00×10^3	.0134

4.3 Propellant modeling limitations in Autodyn

Before discussing any propellant modeling results it is necessary to describe the limitations of solving propellant deflagration simulations using Autodyn explicit dynamics solvers. Autodyn is commonly used to model HE's and hypersonic ballistic projectiles with particle velocities on the order of km/s . In contrast, the burn rates of APCP input to Autodyn have an upper limit of 12.8 mm/s at 8 MPa as tabulated previously in Table 4.2.

This orders of magnitude difference in reaction rates leads to impractical solver times because of limitations on the maximum solver timestep. In a one-dimensional transient finite-difference CFD model with advective flow the maximum difference in solver timesteps is dictated by the Courant-Friedrichs-Lewy (CFL) condition shown in equation 4.11 below.

$$C = \frac{u\delta t}{\delta x} \leq C_{max} \quad (4.11)$$

Wherein u is the velocity magnitude, δx is the width of a single cell, C is the dimensionless Courant number, and C_{max} is 1 for explicit CFD solvers. The velocity magnitude is determined by the speed of acoustic waves traveling through materials in the computational

domain as shown in equation 4.12 below.

$$c = \sqrt{\frac{K_s}{\rho(t)}} \quad (4.12)$$

Wherein c is the soundspeed in the medium and K_s is the bulk modulus of solid materials (or bulk elasticity for fluids). The K_s used in this research was published by Smestad for a pyrotechnic composition as $1.35 \times 10^7 \text{ kPa}$ [27]. Assuming a propellant solid phase density of $1.80 \times 10^3 \frac{\text{kg}}{\text{m}^3}$ (and no gaseous phase) the acoustic wave speed in the solid propellant is equal to $2.739 \times 10^3 \frac{\text{m}}{\text{s}}$. If a 2D model with structured $1 \text{ mm} \times 1 \text{ mm}$ mesh is considered, the maximum allowable timestep for 1D flow through the domain is $3.652 \times 10^{-4} \text{ ms}$. If a larger timestep were used the amplitude of the wave at adjacent cell nodes could not be calculated. Considering the deflagration of a strand of APCP, a sample 10 cm long burning at a constant $12.8 \frac{\text{mm}}{\text{s}}$ and modeled with the same mesh described above would require a minimum of 20 million solver iterations (cycles). In practice the actual number of cycles would increase because multiple acoustic waves are propagating through different regions of material simultaneously at different phases.

To utilize Autodyn for practical modeling efforts the reaction speed was increased via increased convective burn front velocity. The equation for convective burning front velocity present in the slow powder burn EOS is described below in equation 4.13.

$$v = C_1 + C_2 \dot{b}(P_g)(1 + \gamma(\rho_s)) \quad (4.13)$$

Wherein v is the convective burn front velocity, C_1 is an added constant (C_1 is equal to 0 in this research), C_2 is utilized as a density scaling constant, and $\gamma(\rho_s)$ is the solid phase-dependent compaction term. $\gamma(\rho_s)$ is a constant equal to 1 in this research since no experimental compaction data is available for the 3D-printed APCP modeled. Physically, the convective flame front is the transport of gaseous propellant mass to neighboring cells that determines when cell ignition commences as required by equation 4.4. Notice the presence of \dot{b} in equation 4.13; v is equal to the conductive burning rate \dot{b} when C_2 is equal to .5. A solid material with no pores (analogous to a candle burning) will have a C_2 equal to .5

whereas a loosely packed porous material (analogous to a cigarette burning) will have a lower density and higher C_2 because v is able to move through the material with less obstruction. Equation 4.13 is based on Darcy’s law for a fluid moving through a porous medium; if the mass flux through a medium remains constant then an increase in porosity would result in a decreased velocity for a given pressure [28][29]. In this embodiment C_2 is inversely proportional to $\rho_s(t)$, so increasing C_2 indicates the propellant porosity is increasing and v is likewise increasing. A higher v reduces the ignition time for neighboring cells as shown in equation 4.14 below.

$$\tau(t) = \frac{\delta x}{v} \tag{4.14}$$

As v increases $\tau(t)$ decreases. This effect enables neighboring cells to ignite even if the conductive flame front has not entered the neighboring cell yet. Autodyn calculates $\tau(t)$ for an un-ignited adjacent cell and ignites the cell at the given ignition time even if there hasn’t been combusted gaseous phase transport to the adjacent cell. A comparison between conductive burning ($C_2 = .5$) and convective burning ($C_2 = 1,000$) is shown in Figure 4.4 below.

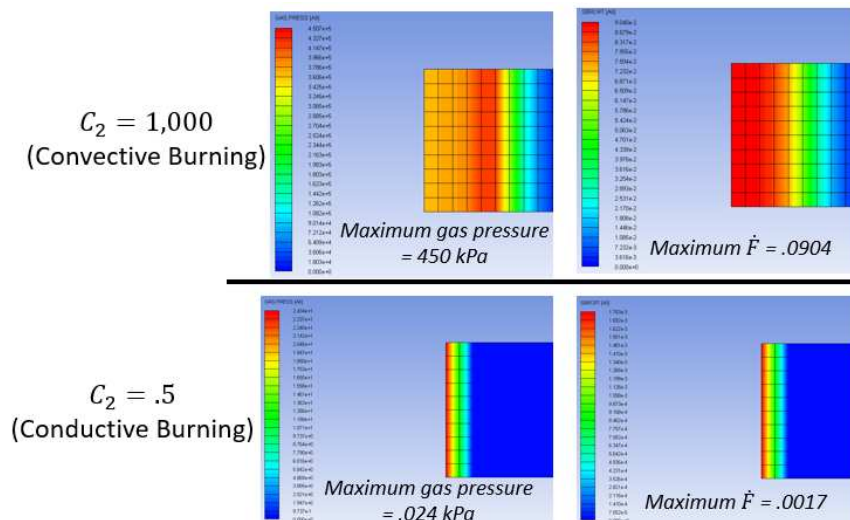


Figure 4.4: Comparison of convective and conductive burning mechanisms on gas pressure and reaction rate in APCP. All contour plots show data at 2.1E-02 m/s after ignition of the first vertical row of cells on the left sides of the Eulerian mesh.

Prior to ignition of any cells in the Euler space the pressure is 0. As deflagration occurs, the gas pressure gradually increases according to equation 4.7. As seen in Figure 4.4 the gas pressure and reaction rate proceed slowly at low pressures. However, in Figure 4.4 the convective burning front has ignited 6 adjacent cells and increased gas pressure 2,000x that of the conductive flame front at the same simulation ending time. Clearly the reactions in high C_2 simulations occur more rapidly than conductive burning simulations and reduce computational time by orders of magnitude.

The drawback to the method described above is that simulations run with high C_2 values give non-physical results when considering complete material deflagration. Since C_2 is inversely proportional to media density, a $C_2 = 1,000$ would produce a v that corresponds to an unrealistic $\rho_s(t)$ of $9E-04 \text{ kg/m}^3$. Changes to C_2 do not affect $\rho_s(t)$ as input to Autodyn as a material property; Autodyn only considers C_2 in equations 4.13 and 4.14. However, simulations with high C_2 do give realistic results for flame front propagation as discussed in 4.4.

4.4 Modeling porosity-graded propellant

One of the primary objectives of this research is to model the effects of porosity on 3D-printed APCP deflagration. Porosity in 3D-printed composite propellant exists as a result of manufacturing defects as previously described in chapter 3. In contrast to manufacturing-defect porosity, meso/microscale porosity may be intentionally introduced to the grain geometry for burn rate manipulation. This subsection presents Autodyn model results for porosity-graded APCP with regions of material at varying fractions of TMD. The results described in this subsection are a culmination of the material characterization research in chapters 2, 3, and of the previous subsections in this chapter.

The porosity data gathered from XCT scan 031219 (as shown previously in Figure 3.7) were used to model flame front propagation in 3D-printed APCP. As previously discussed in chapter 3 the printed samples had varying layer heights due to incomplete polymerization, damage during sample preparation, and general manufacturing inconsistencies due to the

rudimentary AM process utilized for printing the APCP SRM in 2016. This author is confident that current energetics robocasting AM processes are more refined and ensure much higher dimensional accuracy. As such, the layer depth considered in this subsection is assumed to be 1 *mm* as intended during APCP printing.

A single layer segment of porosity data from scan 031219 was used to generate the Eulerian mesh input to Autodyn. The segment porosity concentration was unchanged, but the range of the data set was adjusted to 1 *mm*. The data were then binned into 10 discrete porosity segments along the 1 *mm* layer depth; 4 constant porosity segments were generated along the rising edge to the high porosity region, 1 in the high porosity region, 4 in the trailing edge region, and 1 in the low porosity region. The result gave a discrete histographic porosity segmentation with 10 bins along the 1 *mm* layer depth. A random number generator was then used for random pore placement in each of the 10 porosity segments. The porosity segment considered from scan 031219 and Eulerian mesh input to Autodyn are shown in Figure 4.5 below.

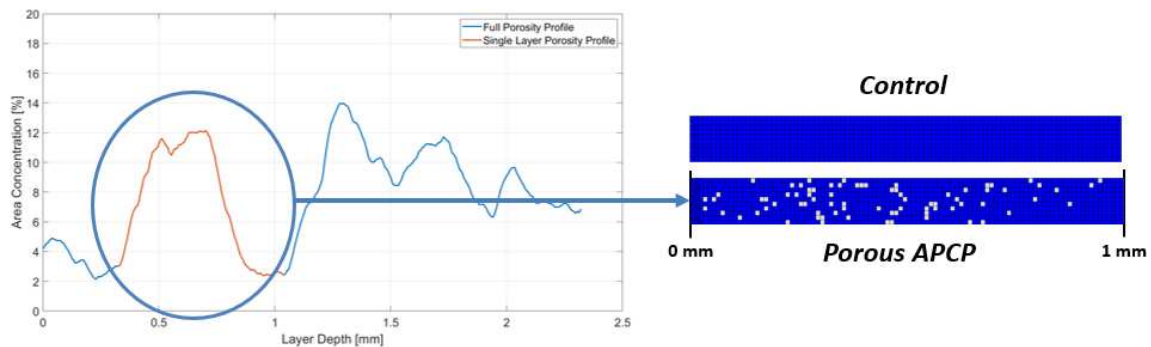


Figure 4.5: Single layer segment of 031219 XCT porosity data used for Autodyn mesh generation. The mesh setup input to Autodyn for porosity deflagration analysis is shown (right). Results from the porous mesh simulation were compared to the control mesh (solid infill) simulation.

The material data input to Autodyn are tabulated below in Table 4.3. Any constants or material data not discussed in previous subsections are referenced from Smestad for pyrotechnic compositions [27]. Burn rate and pressure data input to Autodyn are given previously

in Table 4.2.

Table 4.3: APCP material data for input to Autodyn

$\rho_s(t)$	$1.8 \frac{g}{cm^3}$
Solid Unreacted EOS	Linear
Bulk Modulus	$1.35e+07 \text{ kPa}$
Reference Temperature	293 K
Specific Heat	$0.00 \frac{J}{kgK}$
Thermal Conductivity	$0.00 \frac{J}{mKs}$
Growth parameter G	60 mm^{-1}
Growth reaction ratio exponent c	.667
C_1	$0.00 \frac{m}{s}$
C_2	$1.000e+03$
D	1.869
Energy/unit volume	$3.0543e+06 \frac{kJ}{m^3}$
Strength Model	Von Mises
Shear Modulus	$1.380e+03 \text{ kPa}$
Yield Stress	$2.000e+03 \text{ kPa}$

The simulation setup parameters are tabulated below in Table 4.4.

Table 4.4: Autodyn simulation setup parameters

Initial Conditions	None
Boundary Conditions	None (Closed Bomb)
Part Type	Eulerian
Physical Domain	$1 \text{ mm} \times .1 \text{ mm}$
Mesh Size	$10 \mu m$ (Structured)
Pore Size	$10 \mu m$
Total Number of Pore Cells (Void)	71 (Porous), 0 (Control)
APCP Density (By Volume)	92.9% (Porous), 100% (Control)
Minimum Timestep	$3.400e-07 \text{ ms}$ /cycle (varies)

Note that the control and porous simulation cases only differ in Eulerian mesh setup; the porous case has 71 void cells representing XCT scan porosity, and the control case has 0 void cells representing a sample at TMD.

Since the intent of the modeling was to compare flame propagation through APCP as a function of porosity, the data collected are of the ignition front. As a result, many cells behind the flame front continue to burn and increase in pressure after the front has passed, but those cell data are not considered. Contour plots for transient gas pressure over the domain are shown in Figure 4.6 below.

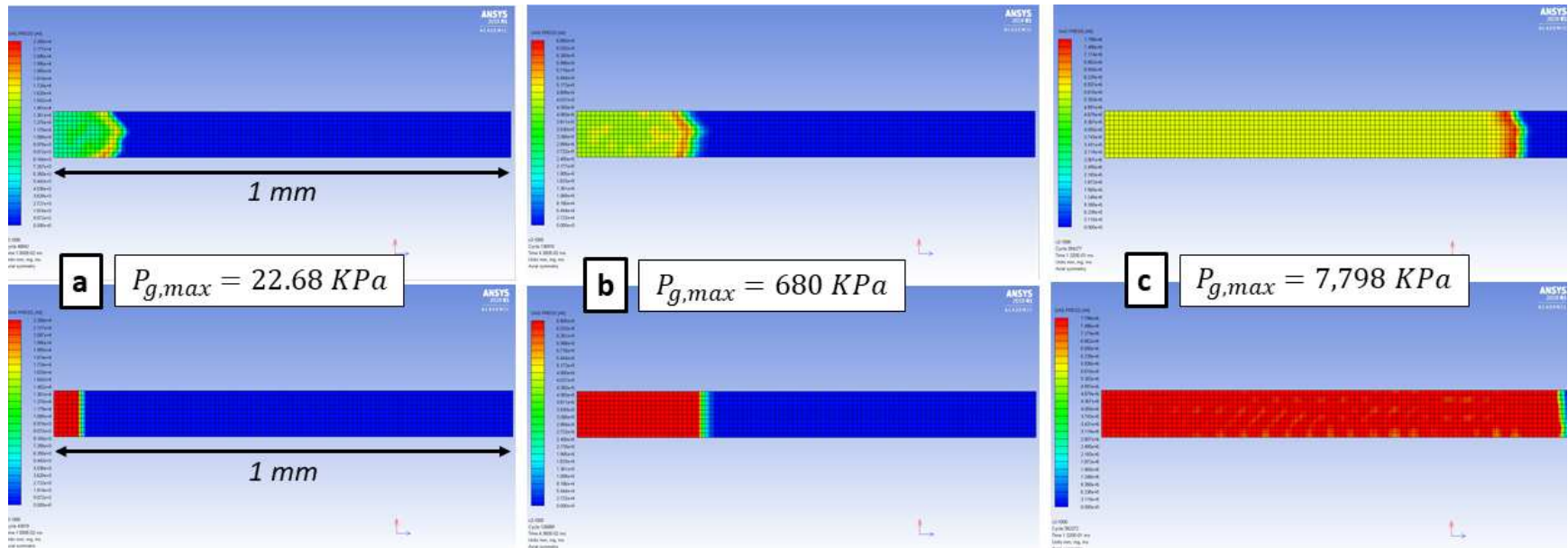


Figure 4.6: Flame front propagation over porous and solid infill APCP. Contour plots for the porous case are shown (top) and plots for the control case are shown (bottom). Contour plots for each case are compared at timesteps $1.50E-02\text{ ms}$ (a), $4.35E-02\text{ ms}$ (b), and $1.32E-01\text{ ms}$ (c). Both cases have equal gas pressure axis scaling at each timestep.

The most obvious difference between the cases shown in Figure 4.6 is the lower gas pressure in the porous case relative to the control case at each timestep. This reduction in gas pressure is likely attributed to compression of the solid propellant phase into empty void cells. As gaseous phase is generated and pressure increases, the solid phase is compressed and the gas is allowed to expand. With more volume to occupy, gas pressure and burn rate remain low even as adjacent cells are ignited.

Since differences in v for the cases are solely attributed to gas pressure (as seen in equation 4.13), v for the porous case is lower than that of the control case, and fewer cells should have ignited in the porous case than for the control case at a given time according to equation 4.14. It is hypothesized that in addition to the cell ignition time delay criteria given in equation 4.14, cell ignition can occur via gaseous mass transport into adjacent cells ahead of v at low pressures.

Burn rate, pressure, and flame front acceleration data from both cases are shown below in Figure 4.7.

As seen in Figure 4.7 the burn rate and gas pressure are lower for the porous case for every position $x > 25 \mu m$. These data further support the hypothesis that gaseous mass transport is an additional ignition criteria to equation 4.14 and that cell ignition in the porous case is dominated by gaseous mass transport at low gas pressures. This hypothesized ignition criteria is in essence Darcy's law and a meso/microscale embodiment of the convective burning front model used in the slow powder burn EOS. Compaction of the solid phase reduces the pore size, increases $\rho_s(t)$ and slows down the flame front. The flame front velocity increases as it encounters porous regions with increased surface area and the flame front accelerates (as shown near $x = .3 mm$ in Figure 4.7).

Also important in Figure 4.7 is the difference in pressures between the control and porous cases seen at ignition of the last cell near $x = 1 mm$. The gas pressure in the control case at ignition time is approximately 17% higher than that of the porous case. Once complete combustion of all cells has occurred, the gas pressure in the control case should be 13.2%

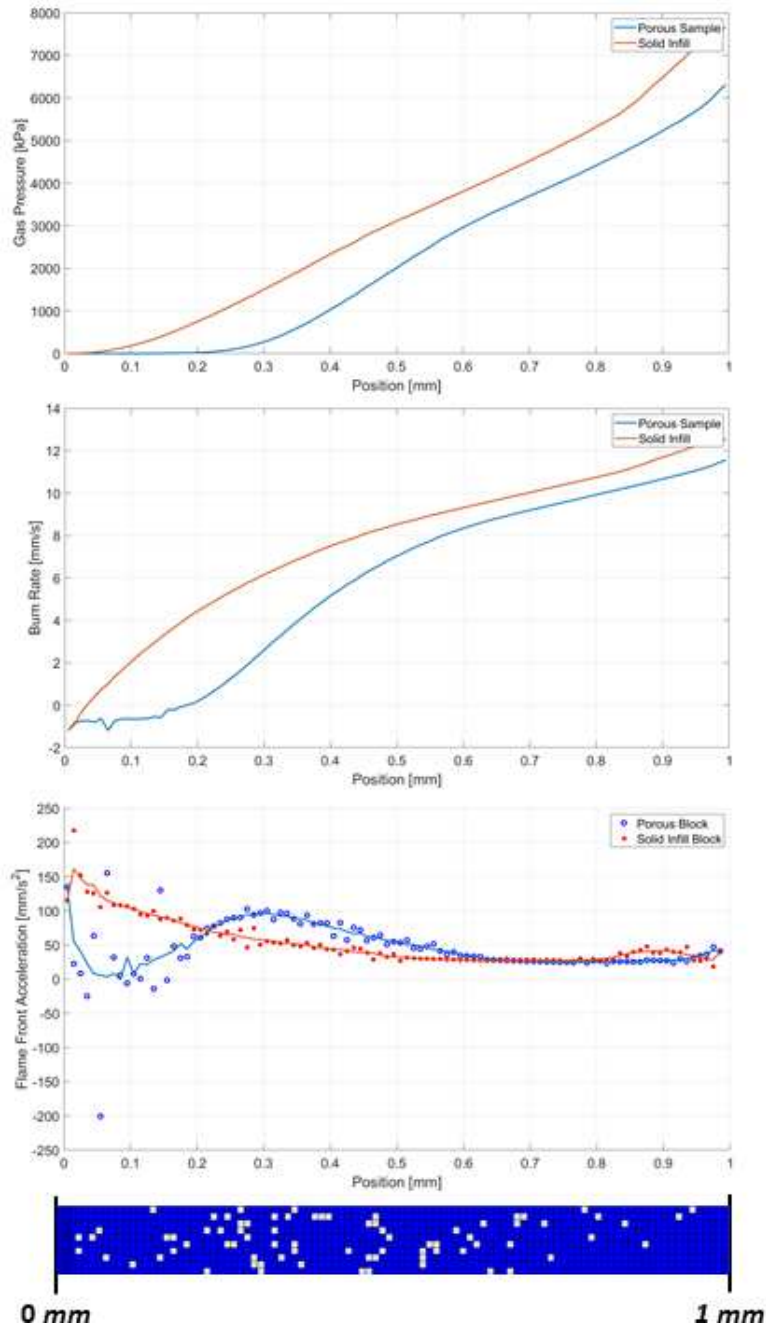


Figure 4.7: Gas pressure, burn rate, and flame front acceleration comparison plots for porous and solid infill APCP. Gas pressure is shown (left), burn rate is shown (middle) and flame front acceleration is shown (right). The Eulerian mesh considered in the porous simulation case is shown for reference.

higher than that of the porous case by equation 4.6. This pressure indicates that more complete cell combustion has occurred in the control case than for the porous case. This result is supported by the higher burn rate (and thus reaction rate) for the control case at every ignition time.

4.5 Summary of Modeling Assumptions

Because the modeling approach was relatively simplistic for solid propellant CFD simulations it is necessary to discuss what impact those assumptions have on the validity of the results.

First and perhaps foremost is that the slow powder burn EOS is not constructed on first principles. Combustion modeling is a highly complex process requiring substantial computing power. The slow powder burn EOS uses experimental data for burn rate and pressure in place of combustion kinetics tool such as CHEMKIN. This assumption means that the rate of complete stoichiometric propellant combustion is captured by equation 4.4. More realistic models would include secondary and tertiary chemical reactions which begin and end simultaneously throughout the combustion process.

Combustion efficiency and reaction rate are captured via experimental data input, but Autodyn cannot model discrete particles. Being that Autodyn is a hydrocode, it models materials as a continuous homogeneous fluid; particulate sizes and micro-scale constituent concentrations cannot be specified. Inevitably, irregularities in the propellant will be introduced during mixing and printing. Defects in the propellant can only be resolved to the minimum cell size in Autodyn. Just as the voids in this research were approximated as single cells in the Eulerian mesh, polymodal particulate distributions, constituent concentration gradients and other characteristics must be assumed as individual cells with unique characteristics.

The slow powder burn EOS does not consider variations in gaseous phase temperature. This assumption implies that the combustion process is approximated as sublimation. Along a phase change boundary the temperature remains constant, so increases in pressure are only

caused by density changes as the sublimating gaseous phase expands around the solid phase. Similarly, the gaseous propellant phase is expanding around the solid phase and pressure increases because the material is defined to the closed-bomb domain. Temperature was neglected in this embodiment of the model because the authors (Atwood) assumed the gaseous phase temperature remains constant at the decomposition temperature and heat conduction between the solid and gaseous phases is neglected [24]. The authors who adapted the model for use in Autodyn (Smestad) then incorporated temperature as a constant in the definition of ideal gas internal energy [27]. Since the thermal conductivity of the gaseous phase is 0, the total internal energy of the system remains constant even after combustion. Assuming a constant decomposition temperature in an isolated system is a valid assumption, but the model will over-approximate internal energy and thus gas pressure in systems with longer reaction time scales where heat transfer through the solid phase or surrounding casing lowers the gas temperature. However, this assumption is also valid for modeling gun propellants where thermal conduction between the gaseous phase and surrounding solid materials is negligible because of the short total reaction time.

If thermal effects are considered, the autoignition temperature of the material must also be considered as an additional cell ignition criteria. In this research, the convective flow through porous material regions was assumed to be at the autoignition temperature (even though cell ignition was actually based on fluid velocity and the calculated timing delay in 4.14). If the flow through porous regions is cooled below the autoignition temperature by the surrounding solid material, propellant ignition will not occur. Thus, Darcy's law may not strictly apply for porous materials; increased surface for the gas to travel over would reduce the gaseous phase enthalpy. The validity of Darcy's law for slow-burning propellants might be approximated by comparing the influence of advective flow to diffusive flow in porous regions via the Peclet number.

4.6 Numerical Modeling Conclusions

The primary objective of this chapter was partially accomplished. An APCP sample with similar density anisotropy to that quantified via XCT imaging was modeled. Differences in deflagration were observed for TMD and porous propellant samples, but conclusions regarding hazardous flame front accelerations cannot be drawn without experimental data for comparison.

At a high level, flame front propagation is dependent on gas pressure and solid phase density in adjacent cells. Lower backpressure and/or increased combusted phase pressure allows faster mass transport to adjacent cells and faster flame propagation in porous regions regardless of the ignition mechanism. Therefore, although convective burning (as calculated in equation 4.13) occurs quicker than conductive burning (as calculated in equation 4.7), the gas pressure present at the convective flame front will be identical to that of a conductive flame front at the time of ignition for a given material geometry per the slow powder burn EOS. The same relationship does not apply for different material geometries; a porous material will compress more than a solid material and backpressure applied to the gaseous phase will be less, but flame front acceleration through porous regions will be higher according to Darcy's law. Model results at low pressures where burn rate is negative are uncertain. As previously mentioned Autodyn corrects the actual burn rate used in calculations to a positive; this is evidenced by the flame front propagation at low pressures where burn rate as calculated by equation 4.7 should be negative. The extent of these auto-corrections are unknown and could potentially be an influential source of error in the results.

The simulation needs experimental compaction data to accurately model APCP deflagration. Since a linear EOS was assumed for the solid phase, compaction will increase with increasing gas pressure. A compaction EOS with non-linear experimental data would change the results seen in subsection 4.4 since $\rho_s(t)$ and gaseous phase flow are dependent on material compaction. Experimental material data are also needed for the specific APCP formulation 3D-printed. The effects of binder concentration gradients in the build direction

are not considered in this research. However, flame front propagation would be impacted by fuel-rich and oxidizer-rich propellant heterogeneity in addition to porosity gradients.

In future research the slow powder burn EOS would be most applicable in modeling small-scale APCP deflagration to determine the effects of meso/microscale porosity on flame front propagation. The use of explicit dynamics solvers for large-scale SRM simulations would not be practical because of timestep limitations imposed by the CFL condition.

CHAPTER 5

CONCLUSIONS

This research characterized defects in 3D-printed APCP related to processing conditions and predicted their effects on propellant deflagration.

The XPS results show relationships between carbon 1s bond concentrations at different analysis depths and validate the initial hypothesis that insufficient UV power transmitted to the APCP slurry during printing caused DOP gradients in layers. The DOP model developed in subsection 2.6 sought to predict DOP at a layer depth as a function of propellant UV attenuation and UV radiation intensity transmit to the surface of the material. Uncertainty in the XPS results was mainly attributed to sample quality, sample preparation, and spectra overlap from neighboring chemical species. Since C=C bond concentration is indicative of photopolymerization in acrylate-terminated polymers it is recommended that alternative spectroscopy methods such as FTIR that are better suited to analyzing C=C bonds be used in future research.

The results produced in chapter 2 helped validate the XCT data in chapter 3. The initial hypothesis that layer delamination in samples was responsible for meso/microscale porosity defects was found to be only partly true; a second mode of porosity generation was found to exist in samples as a result of binder phase separation from solid phase constituents in the composite propellant matrix. Phase separation in samples is thought to have occurred due to insufficient binder wetting to solid particles and low photopolymer cross-linking in the material. A higher DOP would increase photopolymer cross-linking and reduce polymer mobility, thereby reducing the likelihood of binder phase separation over time.

Numerical modeling results produced in Autodyn were consistent with those anticipated for porous material deflagration. Propellant burn rate at the ignition front was modeled along the length of the material via Vielle's law. A high convective flame front velocity

was input to Autodyn to reduce extensive solver times resultant from the CFL condition for explicit dynamics solvers. At a high level, flame front propagation is dependent on gas pressure and solid phase density in adjacent cells. Solid phase material impedance of gaseous mass transport is thought to be the ubiquitous criteria for ignition in Eulerian cells in the slow powder burn EOS. A higher convective flame front velocity will result in faster cell ignition times, but gas pressure in the ignition front is equal for a given cell regardless of conductive or convective-based ignition criteria. The same relationship does not apply for different material geometries; a porous material will compress more than a solid material and backpressure applied to the gaseous phase will be less, but flame front acceleration through porous regions will be higher according to Darcy's law.

The numerical modeling results may potentially be valuable in modeling the effects of porosity in printed APCP on small-scales. Timestep limitations imposed by the CFL condition make Autodyn an impractical choice for modeling deflagration of samples larger than a few millimeters. Importantly, the validity of the numerical model results has not been proven. In this work, the results were not compared to any experimental closed-bomb data, and no existing experimental results comparison literature was found to validate simulations modeled with the slow powder burn EOS. Future research should focus on developing experimental burn rate and pressure data for the specific APCP formulation printed, and on developing experimental compaction data for printed APCP samples for use in Autodyn's solid phase compaction EOS. Autodyn is inherently limiting in this application because it is a hydrocode. The effects of monomodal particulate distribution on deflagration are considered in equation 4.4, but the polymodal particulate distributions commonly used in APCP formulations cannot be accounted for because Autodyn considers fluids as continuous phases; discrete phases cannot be modeled within cells in Autodyn.

Since the samples used for this analysis were printed in 2016, considerable improvements have been made to improve printed SRM DOP, dimensional accuracy, and overall SRM structural integrity. This author does not recommend using PEGDA as a binder for printed

APCP because of the wetting problems seen in this research. Photopolymers used for energetic materials printing should be non-polar and oligomers should have higher molecular weight than the M_n 575 of PEGDA. Although a lower molecular weight reduces the dynamic viscosity in printable APCP slurries, a lower molecular weight also allows for higher polymer mobility in the uncured propellant matrix and a higher tendency to phase separate due to backpressure during printing or interfacial energy gradients.

Additional sources of error in the XPS analysis were realized during the XCT analysis. The concentration of PEGDA at the bottom of the sample as found in XCT imaging likely skewed the XPS DOP results for 1 *mm* layer depth concentrations. The DOP model developed assumed a homogenous propellant formulation, so phase separation was neglected. However, the high PEGDA concentration at the bottom of the layer gave inflated C=C bond concentrations because the propellant formulation was binder-rich and had a higher binder concentration than the surface. The XCT images also found that layer heights varied between 700 μm and 1,000 μm . Since the machine code used for printing specified a 1 *mm* layer height, the layer thickness was assumed to be constant at 1 *mm* for any sample sectioning used in XPS. Samples analyzed in XPS may have unknowingly had varying layer thicknesses and the DOP data gathered may apply for different layer depths.

Sample quality was a recurring problem during sample preparation for XPS and XCT analysis. Samples printed by SAS had 1 *mm* layer depths because of limitations imposed by the printing technology at the time. The positive displacement piston pump utilized for fluid extrusion required steady-state pressure conditions to prevent fluid extrusion irregularities. Heterogeneity and poor binder wetting in the slurry caused problems during printing and necessitated a high flow rate and slow print speed to prevent print failure. Thus, relatively large 1 *mm* layers were used. Attaining complete binder polymerization at depths up to 1 *mm* via photoinitiation alone is unrealistic; the required UV radiation incident to the surface of the material for photoinitiation at 1 *mm* would likely cause ignition of the propellant. As an alternative, this author recommends reducing layer heights to 100 μm - 200 μm and po-

tentially adding a thermally-initiated cross-linker to the formulation if photopolymerization is still insufficient. Severe layer delamination during XCT sample preparation introduced random porosity error to the measurement and reduced confidence in the data set, as in the XPS analysis. It is anticipated that the confidence and repeatability of results in this research would be much higher if samples were printed with the suggested layer heights and binders.

A future embodiment of this research is to intentionally print SRM grains with voids to manipulate the burn rate and thrust of the motor over time as discussed in subsection 1.2. Building on this research and demonstrating repeatability and accurate model prediction of 3D-printed energetic material performance would be a significant advancement in the maturity of this emerging technology.

REFERENCES CITED

- [1] NAROM. The engine types: solid, liquid and hybrid. . . and a fourth, 2018.
- [2] R.A. Braeunig. Rocket propulsion. *Rocket and Space Technology*, 1997, 2005, 2007, 2009, 2012.
- [3] J. Dumoulin. Solid rocket boosters. *Kennedy Space Center, NASA*, 2000.
- [4] Wikipedia. Mesoscale manufacturing, 2008.
- [5] S.F. Son M.S. McClain, I.E. Gunduz. Additive manufacturing of ammonium perchlorate composite propellant with high solids loadings. *Proceedings of the Combustion Institute Volume 37, Issue 3*, pages 3135–3142, 2019.
- [6] E. Hutterer. 3d printing revolutionizes high energetics. *Los Alamos Science and Technology Magazine, Vol. 1663*, pages 2–5, 2016.
- [7] M.J. Mezger K.J. Tindle M. Pantoya L.J. Groven D. Kalyon. *Energetic Materials: Advanced Processing Technologies for next-Generation Materials*. CRC Press, Taylor and Francis Group, 2018.
- [8] A.S. Tappan L.J. Groven J.P. Ball J.C. Miller J.W. Colovos I.J. Cesarano J.N. Stuecker P. Clem. Ldrd final report: Free-form fabrication and precision deposition of energetic materials, 2008.
- [9] J. Wejsa. Ardec energetics at joint armaments conference, 2014.
- [10] B. Dolman A. Hart I. Johnston C. Prior. Advanced munitions: 3d printed firepower. *Defence Science and Technology Group Edinburgh, Australia, 5111*, pages 1–4, 2018.
- [11] S.L. Sanchez. *Study of Polymers Recycling for 3D Printing - PLA Characterization*. Universidad de Cantabria, 2014.
- [12] D.D. Pathak A.K. Mahanta. Htpb-polyurethane: A versatile fuel binder for composite solid propellant. In *Polyurethane*. InTech, 2012.

- [13] L.E. Fried M.R. Manaa P.F. Pagoria R. Randall. Design and synthesis of energetic materials. *Annual Review of Materials Research*, 2001.
- [14] K.S. Mulage R.N. Patkar V.D. Deuskar S.M. Pundlik S.D. Kakade M. Gupta. Studies on a novel thermoplastic polyurethane as a binder for extruded composite propellants. *Journal of Energetic Materials*, 2007.
- [15] E. Tyson. *PLA 3D Printing Filament - Everything You Need to Know*. rigid.ink, 2016.
- [16] C. Brown C. Chewakin M. Feldman A. Lima N. Lindhom C. Lipscomb R. Niedzinski J. Sobol. Solid propellant additive manufacturing (spam). *American Institute of Aeronautics and Astronautics*, 2016.
- [17] U. Orthaber. *Photopolmerization*. University of Ljubljana, Department of physics, 2010.
- [18] CASA. *Quantification for Overlapping Peaks from Different Species*. CASA Software Ltd., 2009.
- [19] C. Decker K. Zahouily D. Decker T. Nguyen T. Viet. Performance analysis of acylphosphine oxides in photoinitiated polymerization. *Polymer* 42, 2001.
- [20] I. A. Aksay J. Lee, R. K. Prud'homme. Cure depth in photopolymerization: Experiments and theory. *Res.*, Vol. 16, No. 12, pages 3538–3543, 2001.
- [21] Y.-H. Ting. The role of cross-linking in surface roughening of polymers during surface etching. *Polymers*, 2011.
- [22] J.A. Arceneaux. Mitigation of oxygen inhibition in uv led, uva, and low intensity uv cure. In Allnex Belgium SA, editor, *RadTech*, 2015.
- [23] A.B. Attygalle A. Svatos. Characterization of vinyl-substituted, carbon-carbon double bonds by gc/ft-ir analysis, 1997.
- [24] A. Atwood E.K. Friis J.F. Moxnes. A mathematical model for combustion of energetic powder materials. In Institut Chemische Technologie, editor, *INTERNATIONAL ANNUAL CONFERENCE- FRAUNHOFER INSTITUT FUR CHEMISCHE TECHNOLOGIE*, 2003.

- [25] J.F. Trubert G. Lengellé, J. Duterque. Combustion of solid propellants, proceedings from internal aerodynamics of solid rocket motor. *Special Course at the Von Karman Institute for Fluid Dynamics*, 2002.
- [26] A.I. Atwood K.P. Ford C.J. Wheeler. High-pressure burning rate studies of solid rocket propellants. *Progress in Propulsion Physics*, 2013.
- [27] E. Smestad J. Moxnes G. Odegardstuen. Modelling of deflagration, establishing material data into ansys autodyn's powder burn model. *International Annual Conference–Fraunhofer Institute Chemical Technology*, 2011.
- [28] S. Verma P.A. Ramakrishna. Dependence of density and burning rate of composite solid propellant on mixer size. *Elsevier*, 2013.
- [29] L. Zhang R. Tian Z. Zhang. Burning rate of ap/htpb base-bleed composite propellant under free ambient pressure. *Elsevier*, 2016.